LOW THRESHOLD RANDOM LASING FROM PHASE SEPARATED OPTICAL FIBERS

BY

SRINATH JAGANNATHAN

THESIS

Submitted in partial fulfillment of the requirements
for the degree of Master of Science in Electrical and Computer Engineering
in the Graduate College of the
University of Illinois at Urbana-Champaign, 2020

Urbana, Illinois

Adviser:

Assistant Professor Peter D. Dragic

Abstract

In this thesis, a low threshold novel random fiber laser, integrating a passive optical fiber with a phase separated aluminosilicate core – silica cladding as the feedback medium, is proposed and presented. The core exhibits greatly enhanced Rayleigh scattering, therefore requiring a significantly reduced length of scattering fiber (4 m) for lasing. The enhanced Rayleigh scattering was verified through measurements and a new figure of merit called effective power reflectivity was also developed to quantify random feedback. With a Yb-doped fiber as the gain medium, the fiber laser operates at 1050 nm with low threshold power, with a tractable lasing wavelength and maximum linewidth, and possesses an output that can be amplified through conventional means. Furthermore, the laser was found to have a high degree of spatial coherence, spectral broadening with increasing input power, and temporal spectral variation. The random lasing action was confirmed both by the use of RF beat spectra measurements and the trends in the Lévy exponent α obtained from the statistics of spectral intensity variation. Cutback experiments carried out shed light on the evolution of lasing behavior with P-SOF length and the impact of feedback on the lasing behavior. The minimum length of P-SOF required for maximum Rayleigh-distributed feedback was also determined to be ~ 2.5 m. This facile setup and results herein pave the way for further study and applications based on low threshold and compact random fiber lasers.

Acknowledgments

A written acknowledgement is not sufficient to express the sheer magnitude of gratitude I have toward the people who have helped me grow both technically and as a person during this journey; however, I would like to take this opportunity to thank the many people who have enriched my experience here. Firstly, I would like to sincerely acknowledge and thank my advisor and mentor Dr. Peter D Dragic. In India, there is an oft used and age-old adage when it comes to a teacher/mentor:

गुरुर्ब्रह्मा गुरुर्विष्णु गुरुर्देवो महेश्वरः |
गुरु साक्षात परब्रह्मा तस्मै श्रीगुरवे नमः |

Roughly translated, it means that a teacher is one who creates awareness, preserves and fosters intellect, destroys ignorance and doubt and is in fact equivalent to the gods, thus deserving of genuine and heartfelt respect. I thank you for embodying every aspect of being a great teacher and mentor as enunciated here and more. Thank you for being so generous with your time, patience and intellect. This work is testament to your guidance and vision. It has been a true joy and blessing working with you and I treasure my memories of you and the group.

I would also like to thank the newly named F.O.R.G.E group for all their support and camaraderie. From group meetings to reviews, you've all been a key part of my journey. Special thanks to all members including Nanjie, Guanyi, Alex V., Alex P., Brian and Liam to name a few. Thanks also to Dr. Ballato's group at Clemson for fabricating the fibers and providing important insights; this work would not have been possible without your contributions.

I would also like to thank my friends both old and new for being there and supporting me through it all. While I may not have said it out loud often enough, your presence and companionship have been a true treasure. Thank you to Aakash, Mukesh, Vignesh Ram, Nilesh, Nitin, Giridar, Joe, Brendan, Corey, Eric, Amit, Alex Pietros and Daniel Viju. Special thanks also to Aniket Murhekar for being a constant, unwavering presence through this process and also for your encouragement and words of wisdom.

Finally, I would like to thank my parents and my sister for being by my side through both the hardships as well as the successes and providing emotional, material and intellectual support. I am truly blessed to have you by my side, and my admiration and love for you all has only grown through my journey here.

Contents

1. Introduction

Random lasers have drawn considerable attention in recent years. This new breed of light source employs optical feedback from random or disordered scatterers as opposed to the conventional approach which makes use of external 'mirrors' [1], consequently forming a well-defined laser oscillator cavity. Random lasers have a host of applications ranging from speckle-free imaging [2,3] to long distance point sensing [4,5], among others [6-10]. Random fiber lasers (RFLs) are one such form of lasers which use fibers and fiber-based components to achieve random lasing. The use of optical fibers as the base provides the added advantage of higher intensity on account of modal confinement and this allows the use to CW fiber coupled semiconductor sources as opposed to extremely high-power pulsed sources which are often bulky. Some RFLs use extrinsic scattering mechanisms for feedback, such as randomized Bragg gratings [11,12], random scattering or reflecting centers [13], or nanocomposite polymer fibers [14]. Other RFLs take advantage of intrinsic scattering mechanisms, including distributed Rayleigh scattering, to provide feedback [15-18]. The RFLs that use Rayleigh scattering as their feedback mechanism typically require long fiber lengths (approximately on the km scale) [16-18] to provide sufficient distributed feedback due to the inherently small degree of Rayleigh scattering in conventional fibers. Consequently, they also make use of distributed nonlinear gain mechanisms, such as Raman amplification, which result in high threshold powers (~W) [15,16,18] and atypical output wavelengths [15,18], and may require the use of pumps with unconventional, or less-common wavelengths [16]. Randomized FBG based RFLs can be short in length and exhibit mode selectivity [11,12], but require specialized post-processing of the fiber in the fabrication of the gratings. Rayleigh-based systems, on the other hand, do not show mode selectivity and are attractive since they require no post-processing, but the aforementioned typically long fiber lengths preclude compactness. While there are subtle differences between the two laser types, the focus of this work is on the latter.

By way of example, integrating a single-mode, 25 km Rayleigh/Raman-based random laser system with a multimode fiber at the output, speckle-free imaging recently was shown [3]. Considering straightforward Rayleigh-based demonstrations such as these, there is a need for a more practical and compact solution that is easy to implement, operates at a low threshold power, and offers versatility in terms of amplification of its output. Thus, there is merit in the development of optical fibers with large-scale scattering to significantly reduce the requisite length of the scattering fiber, while also contending with the other aforementioned requirements. Here, scattering enhancements have been accomplished

through the fabrication of fibers with heterogeneous core compositions resulting from spinodal phase separation of the glass [19]. Coupled with the use of rare-earth-doped fibers as the gain media, these fibers enable the construction of a new kind of compact RFL. Further, since the phase separation is intrinsic to the core composition and naturally occurs during the molten core fiber fabrication [20], the process affords scalability and practicality. Utilizing this fiber, a simple, compact RFL is constructed and explored, and its characteristics including power, spectrum, coherence, and temporal statistics are quantified. The laser utilizes Yb-doped fiber as the gain medium and an FBG reflector, which provides flexibility in the laser emission spectrum. The study and results provided here provide insights into fiber based random laser design based on intrinsic scattering mechanism. Chapter 2 introduces the basic concepts and fundamentals required such as the principles and physics behind optical fibers, Rayleigh scattering in optical fibers, random lasers etc. Chapter 3 deals with the fabrication process, imaging of phase separation and also fiber characterization. Chapter 4 goes into a deep dive of the random fiber laser design setup, characteristics, random lasing action verification and also the cutback experiments. Chapter 5 looks into possible avenues for future work and prospective applications for the proposed design. Chapters 1, 3 and 4 are based on our recently published work in Optics Express (Ref. [21]).

2. Basic Theory and Fundamentals

This chapter discusses the basic concepts and fundamentals relating to optical fibers, Rayleigh scattering in fibers, random lasers and random fiber lasers and ytterbium-doped fibers. Finally, a new approach to constructing random fiber lasers based on fibers with enhanced Rayleigh scattering is introduced which will be discussed in detail in Chapters 3 and 4.

2.1 Optical fibers

An optical fiber is a cylindrical dielectric waveguide that transmits light through the process of total internal reflection (TIR). Essentially it is the transmission of light by confinement due to TIR. A typical exemplar of an optical fiber is shown in Fig. 1. An optical fiber consists of a core, cladding and a buffer. It is the refractive index contrast between the core and cladding that allows for confinement through TIR. Basically, the core must have a greater refractive index than the cladding. This is typically achieved by the use of either index raising dopants in the core like GeO_2 or by the use of index reducing dopants in the cladding like fluorine. It is important to note that the base matrix of commercially and commonly used fibers is silica. The core is the region where the light is guided. A polymer buffer is also used to provide mechanical support and structural integrity. Additional protection through the use of protective jackets is also common especially when used in fiber optic networks. Commonly used cladding diameters are 125 μm and 250 μm and core diameters vary based on their applications. Single-mode fibers typically have diameters ranging from 5 to 10 μm whereas multimode fibers may have core diameters in the range of 10s of μm.

Due to its specific geometry and compositional properties, optical fibers have certain advantages with respect to laser applications. The confinement of light in "modes" allows for high beam quality and diffraction limited beams. Further, this confinement within the core allows for high intensity transmission and light interactions. This is important since many applications become practically realizable on account of high intensities, specifically fiber lasers. Fibers also offer low loss transmission of power which allows for low cavity losses and consequently lower thresholds in lasers. In addition, their low loss suits optical fibers well to long distance, high throughput communication. The versatility of fibers is further evidenced by the ability to reliably dope active gain media into the core. All this allows for fibers to become integrated platforms for lasing among other applications
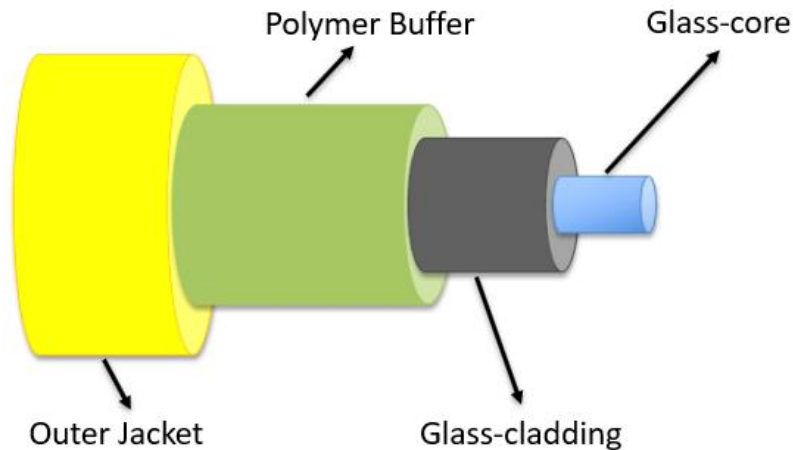
As mentioned earlier, the fibers can be single-mode or multimode. A mode or a transverse mode is basically a self-consistent propagating spatial profile that follows the following condition: the shape of the complex amplitude profile in the transverse dimensions must remain exactly constant. Based on the fiber refractive index distribution and the geometric properties, a fiber may be single-mode or multimode. The 2-D or 1-D (if distribution is radially symmetric) refractive index distribution is referred to as the refractive index profile (RIP). Fibers can further be classified into step index or graded index fibers based on their RIP. Step index fibers have a constant refractive index contrast across the core whereas graded index fibers have radial variation of the refractive index contrast [22]. A pictorial representation of how the RIP looks in the case of a step index fiber as opposed to a graded index fiber is shown in Fig. 2. The possible modes supported by a certain fiber are obtained by solving the Maxwell's equation. While in rectangular waveguides, modes belong to distinct polarizations (TE and TM), in fibers, the modes computed are linearly polarized [LP] (no birefringence) under the approximation that the fiber is weakly guiding (refractive index contrast is very small) and in reality, the approximation holds to a very high degree as well. In a single-mode fiber, only the fundamental mode (LP_{01}) propagates whereas in multimode fibers, higher order modes (HOMs) in addition to the fundamental mode also propagate. However, it is useful to have an easily computable metric which indicates whether a fiber is single-mode or multimode and also if possible estimate the number of modes in a multimode fiber. This metric is called the V number (derived from Maxwell's equation) which is a dimensionless parameter and for a step index fiber is given by [22]:

$$V = \frac{2\pi}{\lambda} \times a \times NA \qquad (2.1)$$

where a is core radius, λ is the wavelength of interest and NA is the numerical aperture which is a measure of the angular acceptance of the incoming light (greater the NA, greater the acceptance angle) which is given by [22]:

$$NA = \sqrt{n_{core}^2 - n_{cladding}^2} \qquad (2.2)$$

However, it is noted that V number is computed differently for a graded index fiber. A V number less than 2.405 indicates single-mode behavior for the given wavelength (there is a cutoff wavelength for the LP_{11} mode, below which the LP_{11} mode begins propagating and single-mode behavior collapses for a given design), whereas a V number greater than 2.405 indicates multimode behavior. The V number is also used to approximately estimate the number of modes in a multimode fiber ($\sim V^2/2$ for a step index fiber and $\sim V^2/4$ for a parabolic graded index fiber) [22]. While commonly used fibers have step index RIPs, fibers generally developed for research possess graded index RIPs [22,23].
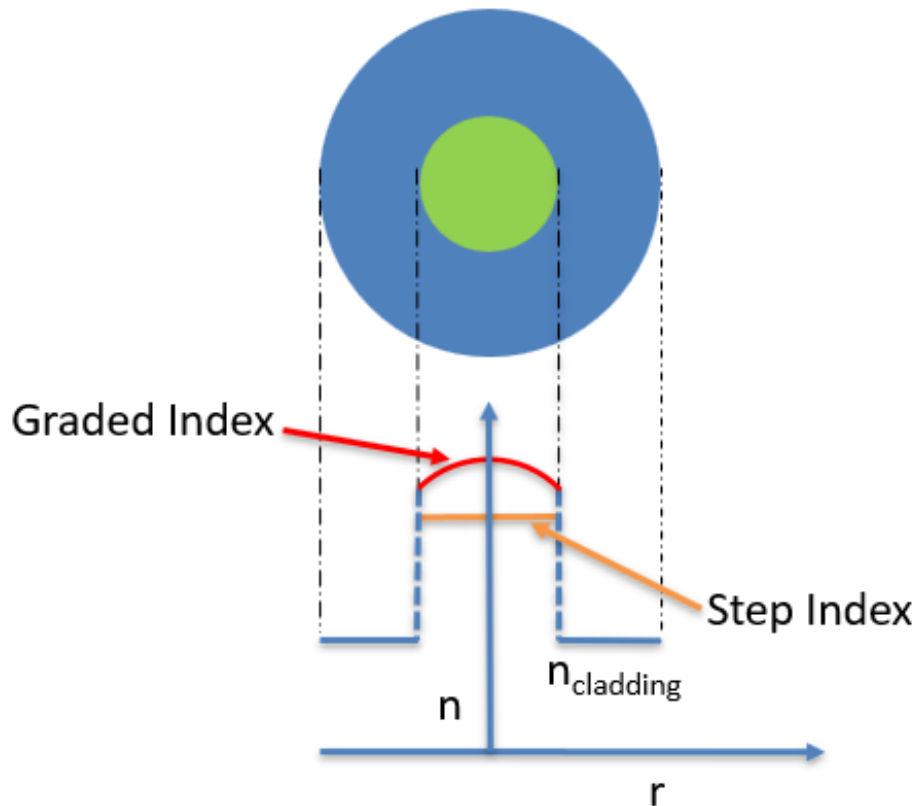

Fig. 2. Comparison between a step index and graded index RIP.

While the V number is enough to estimate the modal properties of an optical fiber, the actual field functions corresponding to these modes as well as the origins of the V number are better understood by solving the Helmholtz equation (derived from Maxwell's equations) in the core and cladding given by:

$$\nabla^2 E + n^2 k_0^2 E = 0 \qquad (2.3)$$

where E is the electric field, n is the material refractive index and $k_0 = 2\pi/\lambda$ is the free space wavenumber. Solving this equation using the cylindrical coordinate system (r, ϕ, z), we get the generalized LP mode field in a step index fiber to be:

$$E_{r,\phi,z} = \begin{pmatrix} AJ_l(pr) & r \leq a \\ BK_l(qr) & r \geq a \end{pmatrix} \begin{pmatrix} sin(l\phi) \\ cos(l\phi) \end{pmatrix} e^{-j\beta z} \qquad (2.4)$$

where $J_l(pr)$ is a Bessel function of the first kind and order l, $K_l(qr)$ is a modified Bessel function of the second kind and order l, and z is the distance in the propagation direction, assuming that light propagates along the Z-axis. The terms p and q can be expressed as follows:

$$p = \sqrt{n_{core}^2 k_0^2 - \beta^2} \qquad (2.5)$$

$$q = \sqrt{\beta^2 - n_{cladding}^2 k_0^2} \qquad (2.6)$$

$$p^2 + q^2 = k_0^2 \left(n_{core}^2 - n_{cladding}^2 \right) \Rightarrow V^2 = a^2(p^2 + q^2) \qquad (2.7)$$

where β is the propagation constant of the wave in the fiber, which is also expressed as $\beta = 2\pi n_{eff}/\lambda$. The parameter n_{eff} is defined as the modal effective index which is essentially the guided mode analog of the material refractive index n. β can be calculated using the boundary conditions, which are continuity of the electric field and its derivative at the boundary. These conditions are imposed based on the weakly guiding approximation and the corresponding equations are listed as follows:

$$AJ_l(pa) - BK_l(qa) = 0 \qquad (2.8)$$

$$ApJ_l'(pa) - BqK_l'(qa) = 0 \qquad (2.9)$$

Eq. (2.8) and Eq. (2.9) can also be illustrated in the matrix form as:

$$\begin{pmatrix} J_l(pa) & -K_l(qa) \\ pJ_l'(pa) & -qK_l'(qa) \end{pmatrix} \begin{pmatrix} A \\ B \end{pmatrix} = 0 \qquad (2.10)$$

For solving this system of linear equations with the variables A and B, the determinant of the coefficient matrix /characteristic matrix must be zero, and this conditional equation can be expressed as:

6

$$qa\frac{K_l'(qa)}{K_l(qa)} = pa\frac{J_l'(pa)}{J_l(pa)} \qquad (2.11)$$

Eq. (2.13) is also known as the dispersion relationship of the fiber. Based on Eq. (2.5), Eq. (2.6) and Eq. (2.11), the propagation coefficient β can be determined. The Eq. (2.11) is a transcendental equation which does not possess an analytic solution, thus the equation is solved numerically. From Eq. (2.7), it is observed that the V number is a dimensionless constant that relates the propagation properties both within and outside the core. Using Eq. (2.7), Eq. (2.11) can be converted to a single variable equation, typically in terms of $p \times a$. This further means that the solution for the propagation constant depends on the value of V, which explains how the V number influences the propagation constant solutions and consequently the number of modes. This method of solving for modes in a step index fiber can be extended to graded index fibers as well by considering the RIP to be an agglomeration of piecewise step index segments. Typical mode intensity profiles along with their LP designation for a few LP modes are shown in Fig .3. The two indices associated with a LP$_{l,m}$ mode are l and m which correspond to the number of radial nodes (l) between lobes and the number of annular nodes (m-1) between lobes respectively. It is also noted that l and l are interchangeable.
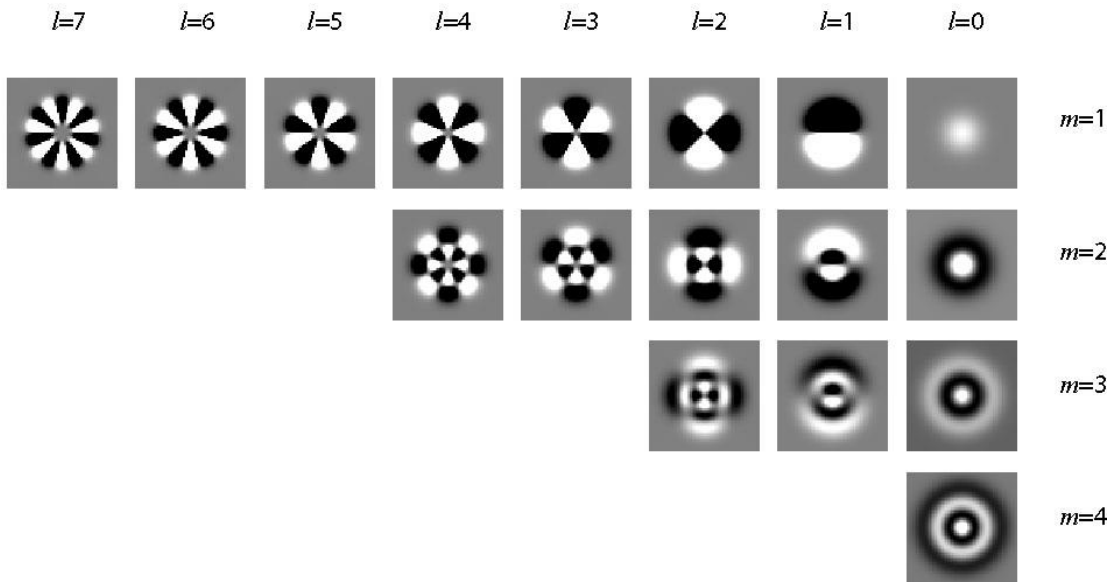

Fig. 3. Modal intensity profiles for LP$_{l,m}$ modes [24].

Modes play a very important role when it comes to power coupling and this can clearly be observed when two dissimilar single-mode fibers interact (fibers are spliced together). In order to quantify the effects of interaction between the modes, a metric called field overlap integral is defined:

$$S = \frac{\left| \int E_1^* E_2 \, dA \right|}{\left(\int |E_1|^2 dA \times \int |E_1|^2 dA \right)^{0.5}}$$

<div align="right">(2.12)</div>

where E_1 and E_2 are the field distributions corresponding to the two modes and A is the cross-sectional area. The square of this field overlap integral is defined as coupling efficiency (η), which basically is a quantitative measure of how well power from one mode couples into the other.

2.2 Rayleigh scattering in fibers

Rayleigh scattering is an elastic scattering process which essentially means that the incident and reflected photons have the same energy and frequency. While propagating in the fiber, light scatters on the random (in strength and position over the fiber, but temporally constant) fluctuations of the density in the fiber core obeying the Rayleigh law. Such density fluctuations are ''frozen'' during the fiber's drawing process. It is important to note that the Rayleigh scattering coefficient [25] and correspondingly its contribution to the overall loss coefficient of a fiber is inversely proportional to the fourth power of the wavelength [26]. In fact, for optical fibers, the spectral loss in dB/Km is given by [26]:

$$\alpha = \frac{A}{\lambda^4} + \alpha_{OH} + \alpha_{IM} + \alpha_{IR}$$

<div align="right">(2.13)</div>

where α_{OH} is the OH absorption loss, α_{IM} is the imperfection loss, α_{IR} is the IR absorption loss and A is the proportionality constant corresponding to the Rayleigh scattering coefficient. Typically, at lower wavelengths, the Rayleigh scattering dominates loss whereas at higher wavelengths IR losses begin dominating. This can clearly be seen in the loss-wavelength plot for a conventional SMF as shown in Fig. 4 ([27]) and the overall loss is minimized at around 1550 nm. This is the rationale for the use of 1550 nm as the wavelength for optical transmission for optical communication systems. Loss also depends on the draw temperature and draw speed, with a slow draw at a lower temperature leading to lower Rayleigh scattering based loss [26].

However, loss is the residual light propagating after scattering as a fraction of the incident light. Feedback is determined by the backscattered light. Rayleigh scattering has an almost uniform scattering angle profile. The angular profile of the scattering is determined by its phase function. The Rayleigh phase function of the scattered light from a particle for unpolarized incident radiation is typically given by [28]:

$$P_{ray}(\theta) = \frac{3}{4}(1 + cos^2 \theta)$$

<div align="right">(2.14)</div>

where θ is the scattering angle. It is noted that this is a good estimate, though more accurate formulae which are more complex have been proposed. The phase function indicates a relatively uniform angular dependence, which can be seen pictorially in Chapter 3 (Fig. 15). So just having strong Rayleigh scattering does not imply strong feedback. In reality, a small part of the light scattered at angles close to π is recaptured by the fiber waveguide and propagates in the direction opposite to the direction of the incident light. The backscattered part of the radiation is equal to $\epsilon = \alpha_s \times Q$ which is an extremely small quantity.
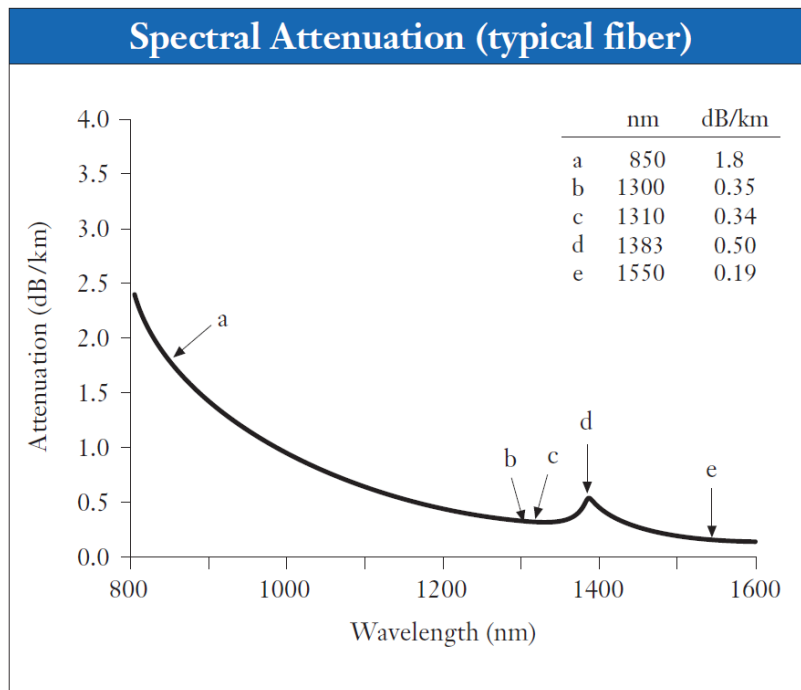

Fig. 4. Loss coefficient (attenuation) in dB/Km vs. wavelength for an SMF-28 fiber. [27]

Here the geometrical factor Q ~ 0.001 is defined by a numerical aperture and geometrical dimensions of the fiber [25]. So, maximizing feedback requires either Rayleigh scattering enhancement or recapture enhancement. Recapture enhancement based on geometry adjustments does not appear to be a good avenue on account of the almost uniform angular scattering profile and the fiber (due to its geometry) only being able to cover a very small portion of this profile. This is also further complicated by the requirement that the recaptured light be confined into guiding modes which further degraded recapture. Thus, Rayleigh scattering enhancement represents the best way forward to maximize feedback. It is also important to note that the size of the inhomogeneities determines the type of scattering that dominates, be it Rayleigh or Mie. Rayleigh scattering dominates when the particle size is smaller than the wavelength (~$\lambda/10$). Thus, a possible approach to boost Rayleigh scattering is to

introduce a large number of small particles/inhomogeneities in the fiber. This is the basic idea behind promoting phase separation in optical fibers which will be discussed in Chapter 3.

2.3 Random lasers and random fiber lasers (RFLs)

Before discussing random lasers, we briefly discuss conventional lasers. Conventional lasers use external mirrors or fiber Bragg gratings (point reflector equivalent on a fiber platform) in the case of fiber lasers to provide feedback. A typical setup for a conventional laser is shown in Fig. 5.
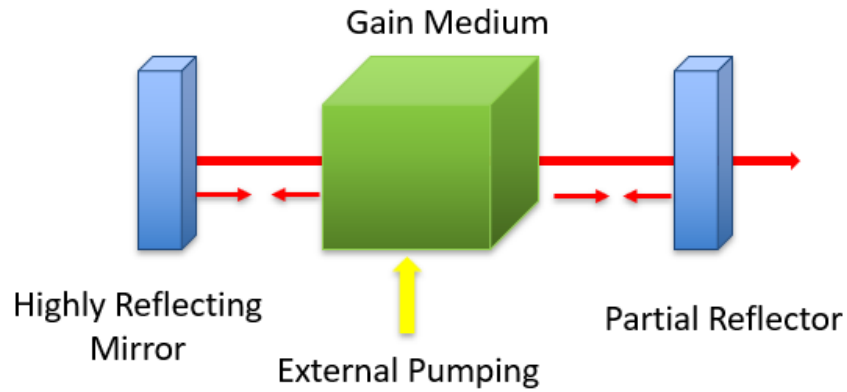

Fig. 5. Setup for a conventional laser (the 2 reflectors bound the laser cavity).

The feedback is coherent and conventional lasers have characteristics imprinted on them by the nature of the cavities used. Principally, cavity lasers have longitudinal modes referred to as cavity modes that are a result of the round-trip phase condition associated with coherent feedback. These cavity modes determine the wavelength/frequency components that constitute the laser spectrum. While typical resolution (in the nm range) associated with optical spectrum analyzers may indicate a broad continuous spectrum, the spectrum is actually comprised of a large number of cavity modes (the number depends among other things on the size of the cavity, the gain spectrum etc.). To observe these cavity modes, either the cavity size has to be very small (~µm) such that frequency spacing is large enough or spectrum of mode beating (RF) must be observed on an electrical spectrum analyzer (much finer frequency resolution). The cavity modes observed in an AlGaN based double heterojunction (DH) laser structure are shown in Fig. 6 [29]. The spacing between consecutive longitudinal modes is referred to as free spectral range (FSR) and is given by [22]:

$$FSR\ (\Delta v) = \frac{c}{2dn} \tag{2.15}$$

where c is the speed of light, d is the cavity size/length and n is the effective refractive index for cavity propagation. The conventional lasers typically have temporally stable spectrum and also exhibit gain narrowing at higher pump powers.
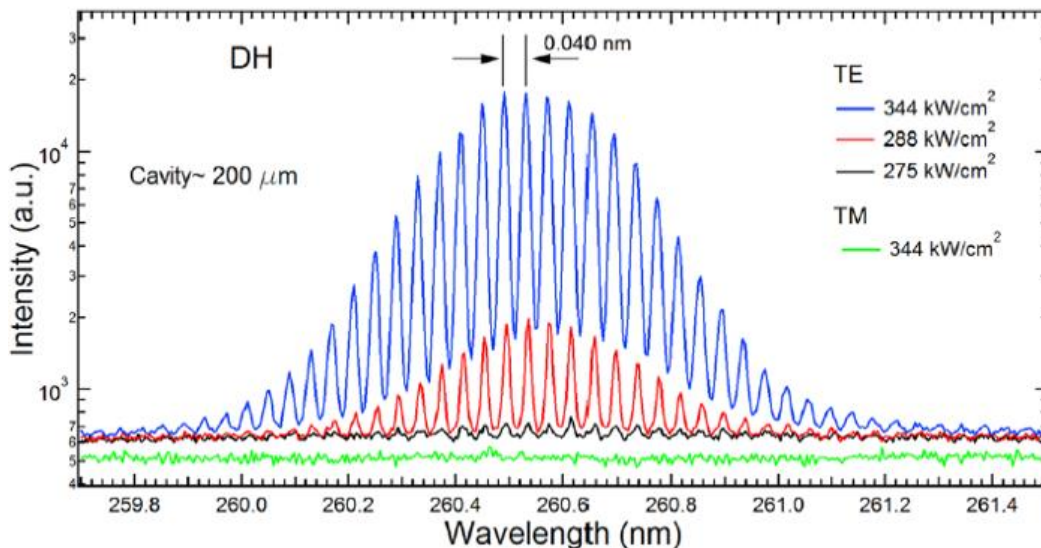

Fig. 6. Polarization-dependent, high-resolution spectra (vertically shifted for clarity) for DH pumped above the threshold (200 µm cavity), the mode-spacing was 0.040 nm, and FWHM of each mode was ~0.014 nm. [29]

Given the wide range of amplifying systems used and the broad scale of materials that are studied in the context of random lasing, a generalized definition is required for what constitutes a random laser. A good definition of a laser is an optical system that satisfies the following two criteria: (1) light is multiply scattered owing to randomness and amplified by stimulated emission, and (2) there exists a threshold, due to the multiple scattering, above which total gain is larger than total loss [6]. In simple terms, a random laser is a laser that uses random or disordered media to obtain partial or complete feedback. The feedback does not necessarily need to be coherent for lasing. Another important point to note is that both localized as well as extended modes can lase though mode coupling is stronger for extended modes. The localized modes also suffer more from gain saturation and are in general harder to come across on account of the tremendous strength of scattering required for the same. Typically, random lasers have some mixture of the scattering particles as well as the gain medium (laser dye) in different configurations. In Fig. 7, a random laser configuration where DCJTB dye-PMMA mixture (gain medium) is spin-coated onto a collection of gold nano-island structures (disordered media) is shown alongside its output spectra [30]. The radiation from the dye molecules is scattered strongly multiple times by the gold nanoislands due to the particle plasmon resonance of the gold nanoislands, where the spectrum of particle plasmon resonance overlaps the emission spectrum of the dye, leading to lasing. It is important

11

to note that population inversion in the gain medium is required for lasing and this is typically done using an optical pump. Nearly all of the non-fiber based random lasers use high power pulsed excitations and the excitation mechanism is also complicated by the fact that pump light gets scattered as well by the scattering media, possibly explaining the high peak power requirements [6].
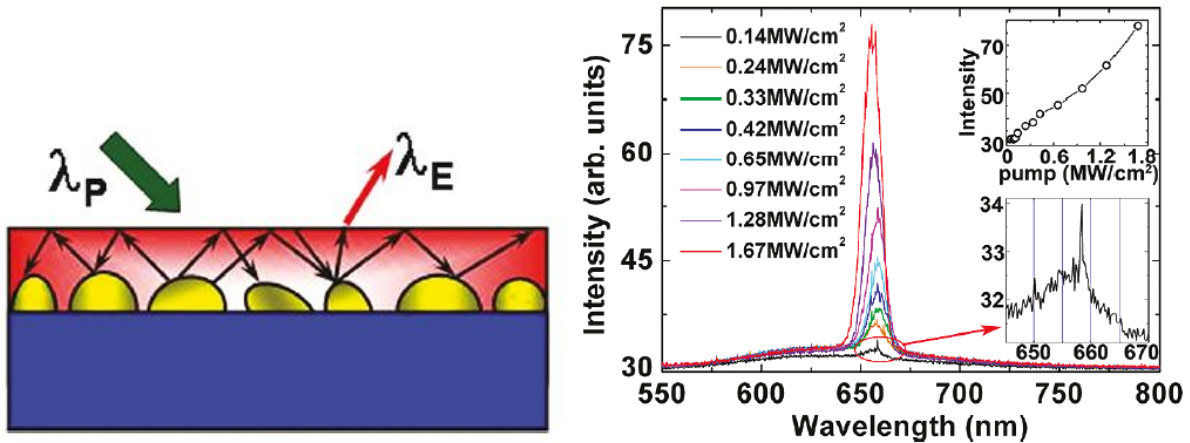

Fig. 7. (L) Illustration of the laser setup (gold nano-islands-scatterers, red region is dye-PMMA solution-gain media/waveguide). (R) Laser emission spectra & Output vs. Input curve [532 nm pulsed pump, pulse width-10 ns, rep-rate-10 Hz]. [27]

Using fiber as a platform adds certain characteristics to a typical random laser. There is definitely transverse confinement (guided modes) and consequently much better spatial coherence especially in the case of single-mode systems. The significantly increased brightness/intensity allows for CW pumping. Random fiber lasers as mentioned earlier can be split into two categories: those that use intrinsically available non-homogeneities as scatterers and those that use extrinsically introduced non-homogeneities (processing done post fabrication) as scatterers. Extrinsic scattering mechanisms predominantly are 1-D arrays of random scatterers [11,12] which though random, exhibit mode selectivity on account of strong latent cavity resonances that impose their dominance over the output spectrum during lasing. They typically do have low thresholds and relatively good efficiencies in addition to being spatially coherent; however, spectrally they are subtly different from the intrinsic scattering based random lasers. While extrinsic random fiber lasers require extensive post-processing which may pose a problem, intrinsic random fiber lasers are easier to fabricate. Intrinsic random fiber lasers for the most part have been dominated by what is termed random DFB fiber lasers or random distributed feedback fiber lasers [31]. The distributed feedback is provided by the Rayleigh scattering and the generally weak Rayleigh scattering means that relatively weak distributed gain mechanisms such as Raman lend themselves very well as the gain providers.

The gain mechanism most commonly used is based on the stimulated Raman scattering. A pump light of frequency v_p incident on a medium excites a quantum of molecular vibrations of the silica glass during an inelastic scattering process and loses some small part of its energy. The residual energy is carried out in the form of a Stokes photon which possesses a frequency $v_s < v_p$ with the frequency difference termed as Stokes shift. The Stokes shift value is determined by a structure of vibration levels of the host media, and the lost energy is manifested in the form of an optical phonon. In the amorphous medium of silica glass with a variety of different collective vibrations, Stokes phonons of the wide energy range following the Raman scattering spectral profile could be spontaneously emitted. It is this spontaneous spectrum that gives rise to stimulated emission. The stimulated Raman scattering rate depends on the pump wave (P_p), and the Stokes wave (P_s) powers and can be described as [31]:

$$\frac{dP_s}{dz} = g_R P_p P_s - \alpha_s P_s$$

(2.16)

where g_R is the frequency-dependent Raman gain coefficient, α_s is the loss coefficient in dB/m and the pump depletion is typically ignored. The various configurations of Raman-Rayleigh based DFB random fiber lasers are differentiated based on the correlation between the direction of the output light propagation and the direction of pumping. So, three schemes are typically seen, which are forward pumped (output and pumping are co-directional), backward pumped (output and pumping are contra-directional) and single-arm configuration. Exemplars for each type are shown in Fig. 8.
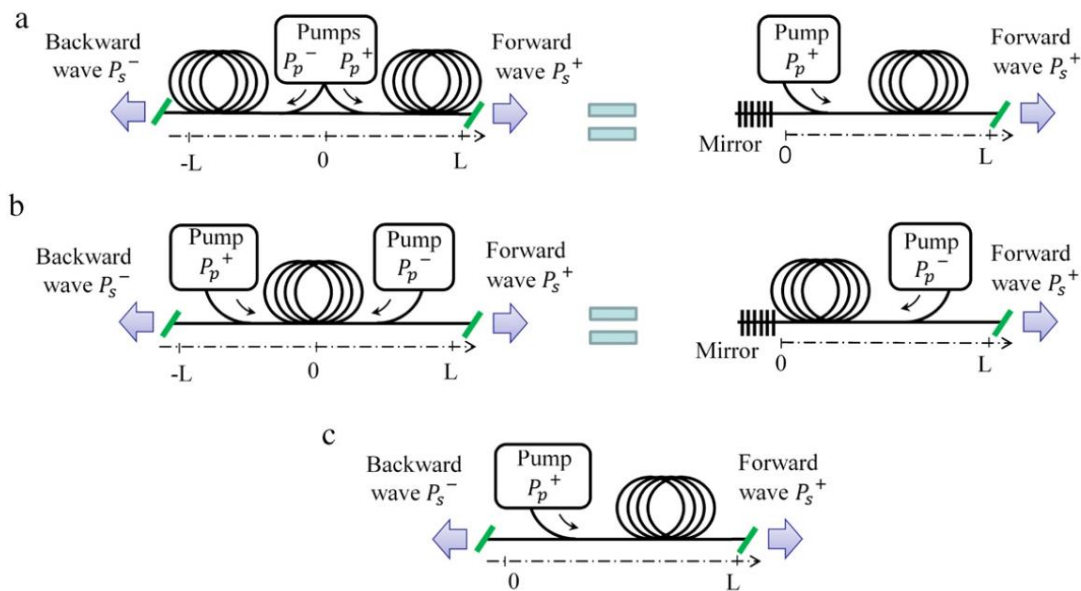

Fig. 8. Random distributed feedback fiber laser configurations: (a) forward-pumped laser, (b) backward-pumped laser and (c) single-arm configuration (angled cleave of 10° at fiber ends to prevent Fresnel feedback). [31]

Random DFB fiber lasers have clear generation thresholds and well-confined optical spectra with a typical width of 1 nm. The output spectra are clearly defined by the gain spectra which in this case is the Raman spectra, and these lasers also tend to show spectral broadening at powers well above threshold. This spectral broadening is a characteristics of conventional Raman lasers [32] as well. These lasers show no peaks in the RF beat spectra (discussed in Chapter 4). They also operate in a quasi-CW regime which is interesting since most conventional random lasers are characterized by intensity dynamics. The output is fairly steady in ms scale [31]. As discussed earlier, random DFB fiber lasers are beset by some drawbacks, which include very high threshold powers, long fiber lengths required and atypical wavelengths. More recently, new random fiber lasers separating the gain medium from the scattering medium [17] have been developed. These lasers are important since they allow for the use of rare-earth-doped fibers as gain media, which in turn allow for further versatility in terms of amplifying the output. It is noted however that many of the issues associated with Raman-Rayleigh random fiber lasers persist, such as high threshold power, long fiber lengths etc. Thus, there is a requirement for a new type of random fiber laser which separates the gain medium from the feedback, but also sidesteps the issues associated with the random DFB fiber lasers.

2.4 Ytterbium-doped fibers (YDF)

Ytterbium-doped fibers are commonly used gain media in fibers and are very versatile. When it comes to fiber-based gain media, it usually involves the active material/ion being doped into the fiber core. Most of the active ions used in fiber gain media are the rare-earth ions found at the bottom of the periodic table such as neodymium, erbium, ytterbium, etc. There are a few reasons why ytterbium as an ion is attractive as opposed to other rare earth alternatives. Firstly, unlike other dopants such as Er^{3+} which have numerous higher energy levels, Yb^{3+} is characterized by a two-level or quasi two-level system. The fundamental advantage of a two-level system is that the process of up-conversion (from the upper state to another higher level) is highly unlikely. Typically, up-conversion is a consequence of clustering [33], which occurs when two active ions in close proximity transfer energy between one another. The amorphous nature of glass means that clumping or clustering is a physical reality. This clustering and the concomitant transfer/sharing of energy means that excitation of ions to higher energy levels, if available, is possible and consequently transition to the ground state from these higher energy levels generate unwanted photons of higher energy (lower wavelength). The observed green emission (~550 nm) when erbium-doped fiber is pumped with a 980 nm laser diode source, when the emission spectrum of Erbium indicates emission at ~1550 nm, is an example of this [34]. Up-conversion strongly degrades laser efficiency, even more so in heavily doped active fibers because the generated photons at

undesired wavelengths take away from expected wavelength emission. The two-level configuration, however, suppresses this up-conversion process and also allows for greater doping concentrations without efficiency degradation due to up-conversion. It is noted from basic laser theory, that a two-level system cannot provide gain and consequently cannot lase. However, Stark splitting [35] explains the degeneracy disintegration of the supposedly two-level system and the two levels $^2F_{5/2}$ and $^2F_{7/2}$ split into three and four sublevels respectively on interaction with the electric field associated with the host (Fig. 9(a)). The two levels are essentially rendered as manifolds, and smearing is also observed on account of the amorphous nature of glass which leads to continuous emission and absorption spectra as opposed to discretized spectra. Transitions between the Stark split components could involve fast phonon generation and annihilation. This allows the YDF to function as a three or four level system, to operate efficiently and consequently to provide high optical gains.
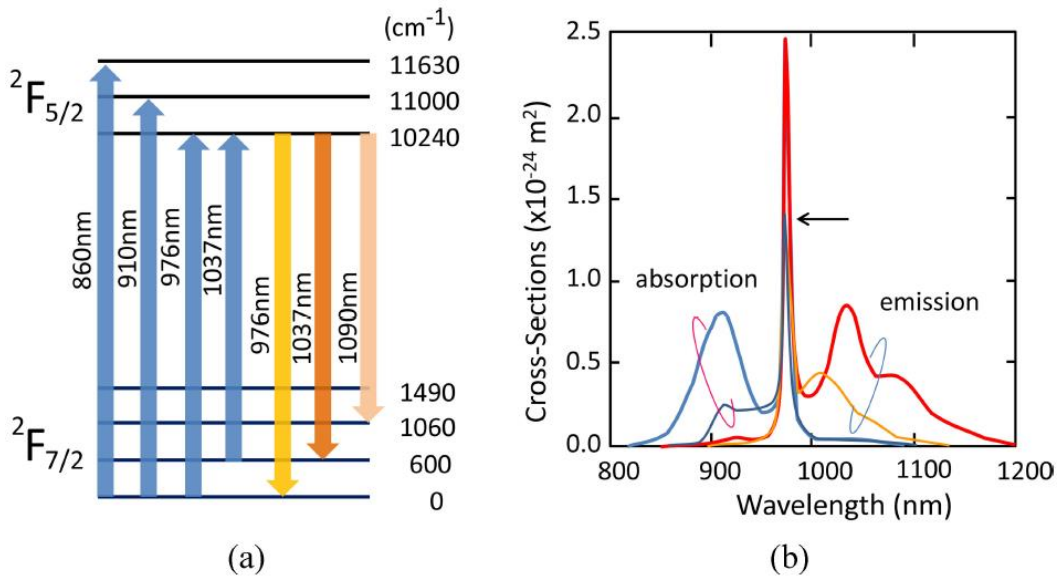

Fig. 9. (a) Typical energy level diagram of Yb3+ ions in silica, (b) typical emission and absorption cross sections in aluminosilicate (thicker lines) and phosphosilicate (thinner lines) fibers (the arrow shows the peak emission and absorption for phosphosilicate fibers). [35]

The typical emission and absorption cross sections of a commercial Yb-doped aluminosilicate and phosphor-silicate fibers are shown in Fig. 9(b). The aluminosilicate fiber (typically used for lasing application) has the zero-phonon line around 976 nm, absorption local maximum around 920 nm and emission local maximum around 1030 nm. The phospho-silicate fiber has the same zero phonon wavelength but different local maxima with reduced cross sections (used for highly doped case). The effect of the host on the resulting cross sections is clearly observed. The YDF is found to have much larger emission and absorption cross sections as compared to other active fibers (approximately five

times that of Er-doped fiber and approximately three times that of Tm-doped fiber). The upper state lifetimes of ytterbium doped gain media are also found to be relatively long (typically of the order of 1-2 ms), which allows for significant inversion to be achieved at low pump powers. The larger cross section coupled with the possibility of greater Yb^{3+} doping allows for greater gain realization in YDF based systems.

2.5 A new approach?

The focus of this work is on random fiber lasers that use intrinsic scattering mechanisms for feedback. It is evidently clear based on the previous discussion that a new approach to random lasing with intrinsic feedback is required. What is required is a fiber with enhanced Rayleigh scattering in order to maximize backscattering feedback and minimize the length of the fiber required in the setup. This is in order to make the lasing system compact. The separation of the gain medium and scattering medium is also eminently desired in order to use easily available and versatile rare-earth-doped fibers for gain instead of weak non-linear effects like the Raman effect. Enhanced Rayleigh scattering based feedback also requires gain medium separation since if the Raman-Rayleigh combination were to be used, the cavity losses would be excessive and the effective length (L_{eff}) would be drastically reduced, consequently degrading distributed gain. It is important to note that the inverse relation of Rayleigh scattering strength with wavelength means a lower wavelength would be preferable. Additionally, YDF would be preferred as the gain medium on account of its ability to provide high optical gain. This is especially important when attempting a novel setup where parameters may not be well optimized. The use of YDF would also allow for the use of commonly available fiber coupled semiconductor lasers at 976 nm and would also allow for output amplification. While Er-doped fiber (EDF) also has similar advantages, the need for high optical gain and lower output wavelength clearly indicates that YDF (1050 nm output) would be a much better choice than EDF (1550 nm output) for a comprehensive study. With YDF as the gain medium and enhanced Rayleigh scattering based feedback on one side, a conventional reflector providing feedback on the other end would also be desirable. This is because while enhanced Rayleigh scattering is good for feedback, it clearly degrades the through signal/output. So, using a FBG on the other end (output end) to provide feedback would definitely improve the output characteristics considerably. The FBG would also allow for some degree of control on the lasing spectrum (basically the linewidth) and could in theory also be an optimizable component to improve lasing power characteristics. Here, a rough skeletal model and the rationale behind it have been provided. Further detailing and actual implementation will follow in Chapter 4.

3. Phase Separated Optical Fibers (P-SOF)

This chapter discusses the fiber fabrication process and fiber characterization. First, the fiber fabrication is discussed briefly to provide insights on the dopants used, the actual process and the output of this process. The phase separation is then visually observed using high resolution imaging. Thereafter, the fiber properties including the RIP, the modal nature and properties, and the type of scattering that dominates are discussed.

3.1 Fiber fabrication

As enunciated earlier, a phase separated optical fiber is basically an optical fiber with a core where the dopants exhibit phase separation. Firstly, the fiber fabrication process is discussed briefly. The fiber to be used was fabricated using the molten core method (MCM) [20]. In short, pure alumina (Al_2O_3) powder was inserted into a telecommunications-grade silica capillary preform tube (3 mm inner / 30 mm outer diameter) that serves as the fiber cladding after drawing. This powder-in-tube preform then was drawn at a temperature of about 2100 °C. At these temperatures, the core melts, and the silica cladding softens, enabling a direct transition to fiber. As SiO_2 from the cladding dissolves into the molten core during the draw, natural immiscibilities in the $SiO_2 – Al_2O_3$ system lead to heterogeneities in the resultant core as the fiber is drawn and cools. The fiber was drawn with a targeted cladding diameter of 125 μm, and coated with a UV-curable conventional acrylate, yielding a total fiber diameter (including the buffer) of approximately 250 μm. It is noted that the conventional geometry of this fiber design provides the additional advantage of easier splicing with commercially available fibers and fiber-based components. By taking advantage of the draw conditions during fiber fabrication (essentially draw temperature in this case), nano-scale phase separation could be promoted in these fibers possessing cores with lower silica content, by conventional fiber compositional measures [19]. More details on the phase separation process can be found in Ref. [19], where this was investigated for the aluminosilicate system. In Fig. 10, the nanoscale phase separation in the case of the fabricated alumino-silicate fiber is shown. Spinodal phase separation is apparent in the aluminosilicate fiber, with darker granular regions indicating areas of greater Si concentration relative to Al [19]. No such nano-structuring is apparent for the pure silica cladding region. It is noted that in this case, based on the draw conditions and dopant chosen, spinodal phase separation is observed. However, a calcium silicate fiber drawn similarly exhibits Binodal phase separation (shown in Fig. 11). Binodal decomposition results in a metastable state and comprises of a broader region of immiscibility (nucleated morphology observed), whereas spinodal decomposition results in an unstable state and leads to a specific microstructure (wormlike morphology observed) [36].
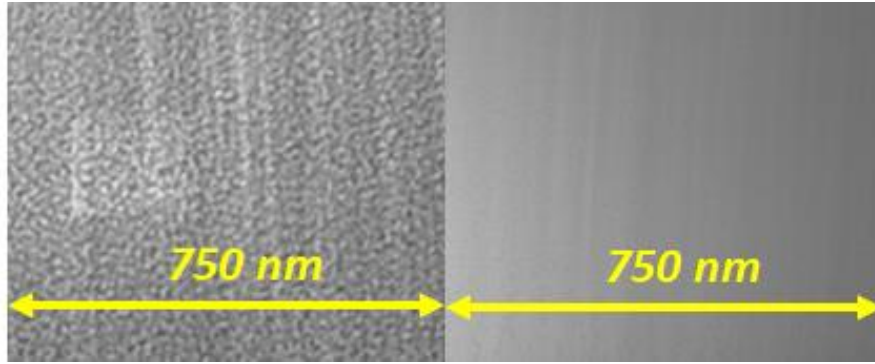
Fig. 10. Scanning transmission electron microscope (STEM) image of the aluminosilicate fiber core (left) and pure silica cladding (right).
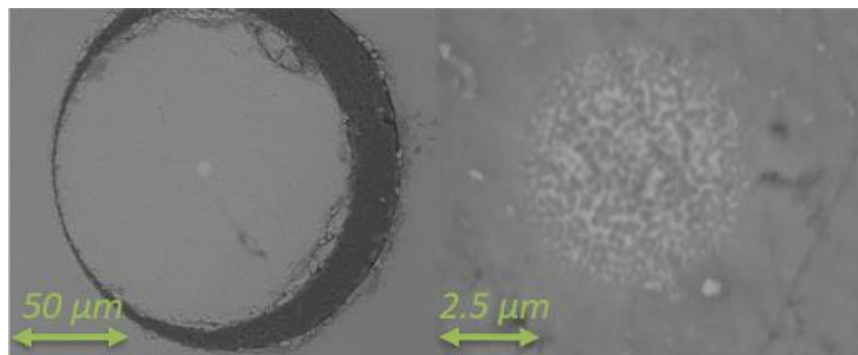

Fig. 11. Scanning electron microscope (SEM) image of the calcium-silicate core-cladding (left) [~5 μm core dia] and calcium silicate core (right) [particle size of the order of 250 nm].

3.2 Fiber characterization

Phase separation was observed via electron microscopy. In short, glass core and cladding slices were milled using a focused ion beam coupled with an electron beam microscope (HITACHI NB5000) and thinned down to a 100 nm thickness. Subsequently, the same HITACHI NB5000 was set in a scanning transmission electron microscope configuration (STEM, Bright Field mode, 30 kV) and the nanostructures arising from phase separation were observed. In this case, it was found that spinodal phase separation (shown on the left side of Fig. 10) dominates in the fabricated aluminosilicate core optical fiber. The resulting attenuation of the P-SOF was determined to be ~18 dB/m at 1050 nm (lasing wavelength) which can principally be attributed to scattering, although some absorptive impurity loss likely also is present [37]. For the calcium silicate case, SEM (scanning electron microscope) was used to observe the phase separation from a lateral cross section.

The refractive index profile (RIP) was measured transversely through the side of the fiber at a wavelength of 980 nm using a spatially resolved Fourier transform interferometer [38] and is shown in Fig. 12. The core composition was determined using energy-dispersive X-ray analysis (EDX) and is also

18

provided in Fig. 12. The core was found to contain only alumina and silica, as expected. The maximum refractive index difference, taken between the fiber core center and its silica cladding, was measured to be 0.0587, and the maximum alumina molar concentration was found to be ~ 19.7%. The diameter of the core was estimated to be about 16.2 μm from the RIP line-scans.
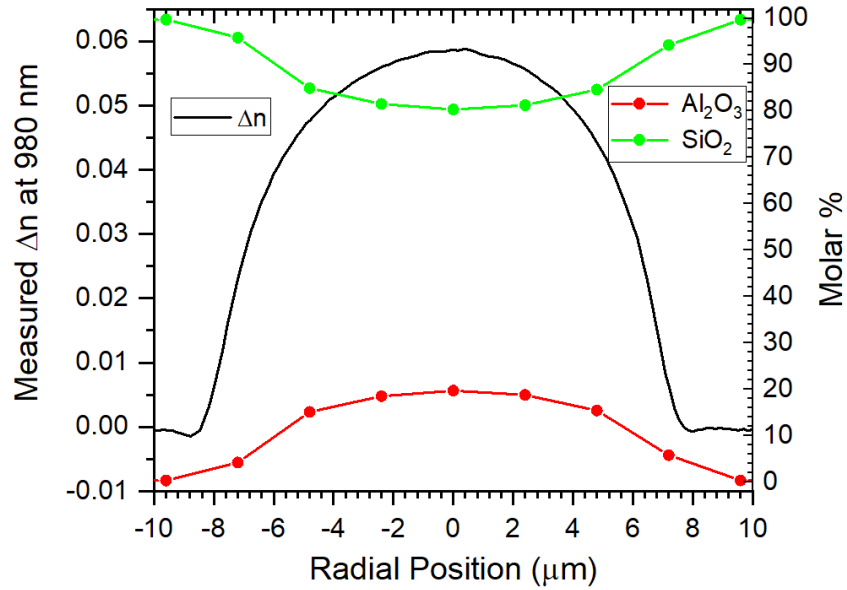

Fig. 12. 1-D linescan extracted from 2-D RIP data and the molar composition in the fiber core from the EDX measurement as a function of the radial position.
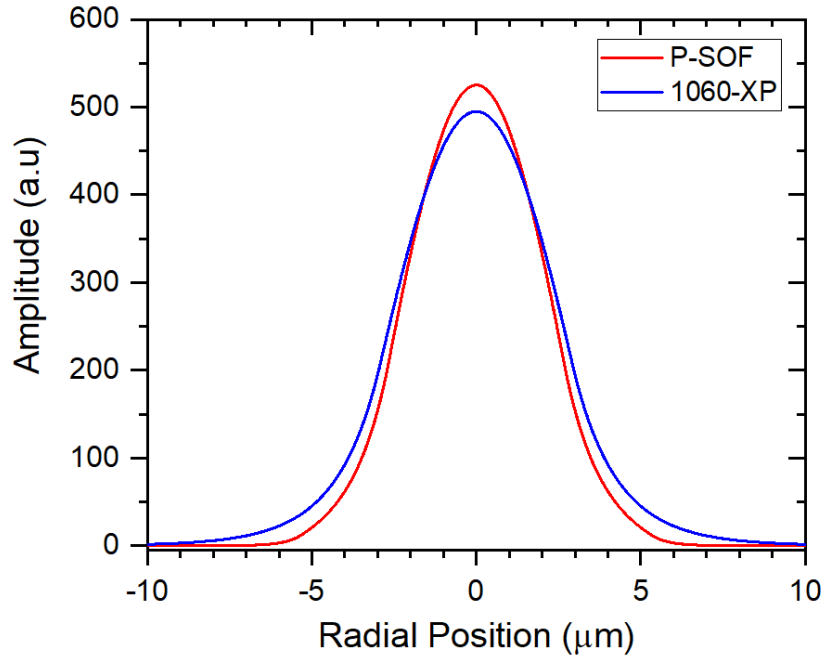

Fig. 13. Modal overlap between the fundamental modes (LP$_{01}$) of the P-SOF and 1060-XP fiber [Mode profiles simulated using RIP data, integrated power normalized].

Using the RIP data, modal analysis of the P-SOF was performed using an in-house solver to further understand the fiber's mode distribution. Of particular importance is the implication of mating this fiber with a conventional single-mode fiber in the laser system, specifically with 1060-XP (Coherent-Nufern, USA), which is hereafter referred to as the 'connecting fiber.' At a wavelength of 1050 nm, the P-SOF was confirmed to be multimode although the overlap between the fundamental (LP_{01}) modes in the 1060-XP fiber and in the P-SOF was found to be very high (~ 99.1%), as can be discerned from Fig. 13. The P-SOF at 1050 nm has about 30 modes and a fundamental mode diameter of 5.504 μm (assuming the weakly guiding assumption to be valid). While the fundamental mode could efficiently be excited upon launching into the P-SOF, strong Rayleigh scattering is expected to couple the LP_{01} mode quickly into higher-order modes (HOMs), both in the backward and forward directions. This indicates that the overall loss is dominated by the return feedback path from the P-SOF, principally due to mode mismatch losses post-scattering (Rayleigh dominated as shown in Fig. 15). A P-SOF designed to have fewer modes, or, ideally, to be single-mode at 1050 nm, could significantly improve the performance of any integrated lasing system based on feedback from such phase separated glass cores. However, this can be challenging, as it is the large concentration of alumina, an index-raising dopant (greater NA), that facilitates phase separation.

The nano-scale phase separation observed in the core from the STEM images indicates that scattering should be dominantly Rayleigh, as opposed to Mie, near the lasing wavelength (~ 1 μm). In order to confirm this conjecture, a scattering profile was measured. More specifically, a segment of fiber was passed axially perpendicular across an aperture (with 1 mm diameter) and green light from a 532 nm doubled Nd:YAG laser was launched into one end. The spatial intensity pattern emerging from the aperture then was characterized by using a Si detector that was attached to a rotation stage (with angular positions, θ, of 0° and 180° representing scattering in the forward and backward direction, respectively). This secured equidistant rotation of the sensor about the aperture. A pictorial representation of the setup is shown in Fig. 14. It is noted that there is a distinct reduction in scattering at smaller angles on account of fiber recapture of light and the fact that measurement of scattered light at very low angles is hindered by the mechanical constraints of the system. The result of this measurement (normalized) is shown in Fig. 15. The angular dependence of the theoretical normalized Rayleigh scattering intensity (I) as discussed in Chapter 2 (Eq. (2.14)) is reformulated and given below.

$$I \; \alpha \; 0.5(1 + cos^2 \theta) \tag{3.1}$$

Eq. (3.1) is plotted in Fig. 15, visually demonstrating good agreement with measured data. To further quantify this, the equation ($f(\theta) = \alpha(1 + \cos^2 \theta)$) was fitted to measured data (θ from 40°-140°) via the nonlinear least squares method. The value of the proportionality constant, α, was found to be 0.491 with a corresponding adjusted R-square value of 0.915, indicating a good fit and thereby pointing to the dominance of Rayleigh scattering in this fiber.
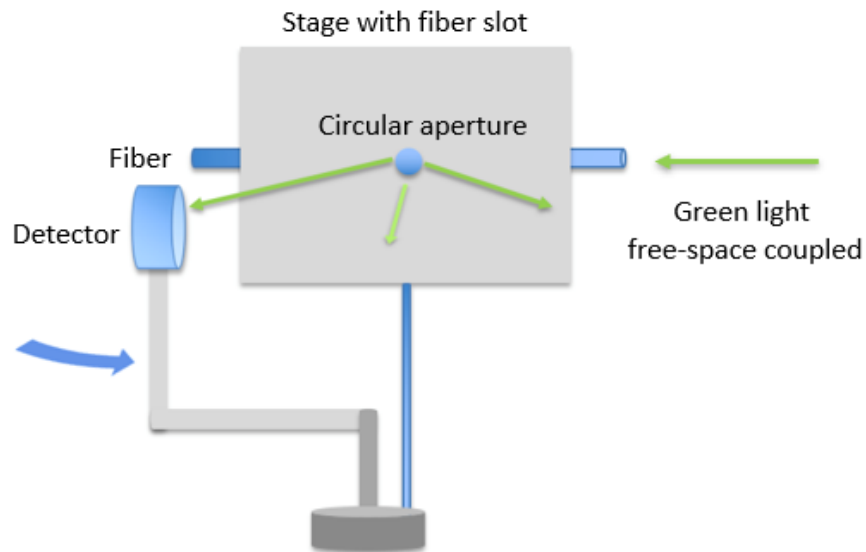

Fig. 14. Setup to measure normalized Rayleigh pattern [scattering signal →0 for 150° < θ < 30° due to fiber capture].
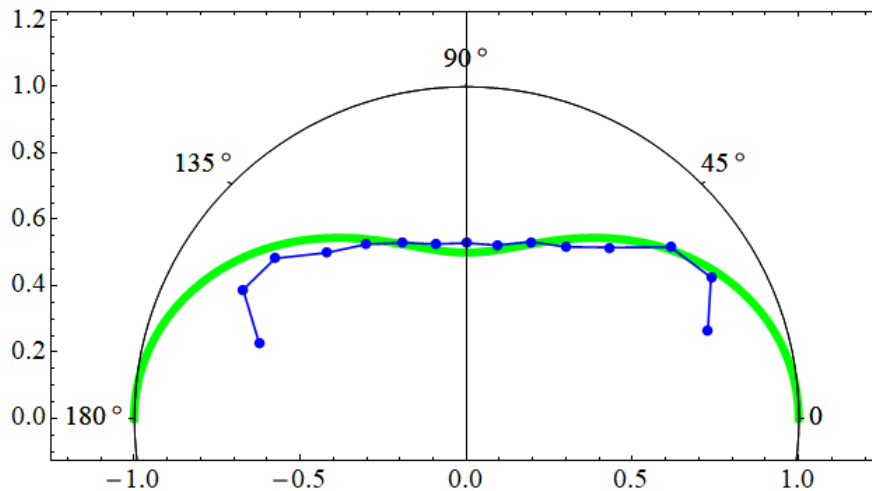

Fig. 15. Normalized scattering pattern measured at 532 nm for the P-SOF (blue) and the normalized Rayleigh pattern from theory (green). The reduction in scattering approaching 0° and 180° is due to recapture of the scattered light by the fiber.

4. Low Threshold Random Fiber Laser Based on P-SOF

This chapter discusses the practical implementation of the design conceptualized in Chapter 1. Thereafter, it discusses the laser characteristics (power curve, temporal, spectral and coherence characteristics). It also discusses experimental confirmation of random lasing action (RF beat spectra and spectral intensity statistics). Thereafter, the results of cutback experiments performed (both angled and flat cleaved) are discussed. This chapter provides a comprehensive understanding of the random laser performance and also develops theoretical and simulation-based constructs like R_{eff} to understand the RFL better.

4.1 Random laser setup

As will be shown, the enhanced Rayleigh scattering in the P-SOF allows the use of a relatively short length of the P-SOF for distributed random feedback and enables the separation of the gain medium (commercial Yb-doped fiber, YDF) from the feedback medium. Integrating a YDF (or a rare-earth-doped fiber, generally) for gain also offers the possibility of amplifying the output using successive YDF-based amplifying stages. Turning now to the laser configuration, Fig. 16 shows a block diagram of the setup. A 75 cm length of commercial single-mode YDF (Liekki, Yb 1200-4/125 fiber, Thorlabs USA) is pumped through a wavelength division multiplexer (WDM) by a single-mode fiber-coupled laser centered at 976 nm (Lumentum, USA). The length of YDF used was optimized via a cutback process which aimed to maximize the output power and the slope efficiency. The use of the specific fiber coupled source ultimately constrained the maximum power that can be launched into the system to less than 1 W. Feedback at the output end is provided by a fiber Bragg grating (FBG, 50.68% reflectivity, 1049.78 nm center wavelength, and 1.199 nm spectral width, O/E Land, Canada). The FBG is used to select the output wavelength as well as to control the maximum linewidth achievable by the random laser. The feedback from the other end comes from either (A) flat-cleaving the WDM fiber, which essentially acts as a 3.4% Fresnel reflector, or (B) the spliced P-SOF. The former (Case A) was used to establish a benchmark non-random laser for comparison purposes. In the case of the latter (Case B), the fiber length is simply chosen to be long enough (4 m) such that no light emerges from the back-fiber facet. This is done essentially to ensure that maximum feedback is provided by the P-SOF and the impact of the end facet is minimized. Splicing is performed with a standard telecom splicer for all fibers composing the system, including that between the WDM and scattering fiber.
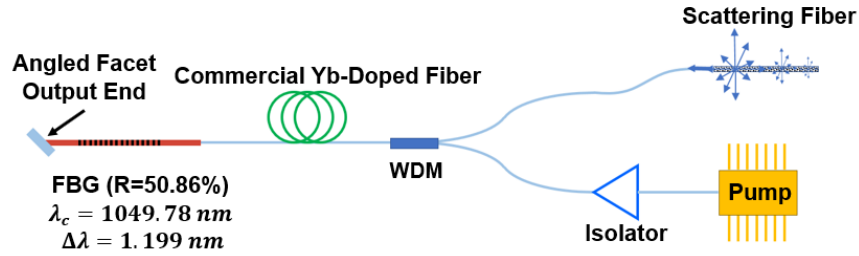
Fig. 16. Random laser configuration. The commercial Yb-doped fiber (YDF) is end-pumped by a laser diode operating at 976 nm and the output is taken at the FBG end. An isolator was used to prevent parasitic system lasing from the pump laser facet.

4.2 General lasing characteristics

The output power versus input power curves for the two cases (A and B as defined earlier) are shown in Fig. 17. The input power is defined here as the pump power entering the Yb-doped fiber after taking the mode mismatch loss (coupling efficiency theoretically estimated to be 87.4% in going from the WDM to YDF) into account. The random laser was found to have significant amplified spontaneous emission (ASE), and this power was integrated (ASE power fractions ranging from 0.31-0.36 at input powers well above P_{th} [P_{in} > 4P_{th}]) and subtracted from the measurement to provide strictly the lasing output power as shown in Fig. 17. The significant impact of ASE is on account of the low slope efficiency and consequently low lasing power in the pump power regime used. In the case of the random laser (with P-SOF, Case B), observed was a threshold power (P_{th}) of 62.1 mW and a maximum output power of ~ 3.3 mW. The low slope efficiency (1.31%) is primarily due to the intrinsic loss associated with the P-SOF and mode mismatch loss between the P-SOF and connecting fiber (1060-XP), as described in Chapter 3. It is also noted that for both cases, most of the optical power exits not through the output (FBG) end, but rather through the back end of the system. For Case A, this is a flat-cleave with approximately 96.6% transmission, so the power exiting the back end of the laser is roughly equal to the intracavity power. In the case of the P-SOF, this light is scattered from the fiber in a pattern governed by Eq. (2.1). This scattering ensures that the actual power exiting the P-SOF is minimal and thus, though there is significant power entering the P-SOF, it is not usable so to speak. The significant scattering also allows for visual confirmation of lasing based on the light scattered from the P-SOF saturating the detector of the Fujikura splicer (Fig. 18).

To further understand the lasing characteristics, a model based on Ref. [39] was developed. This application generates slope efficiency (η) and P_{th} using the YDF characteristics, YDF length and feedback reflectivity values as inputs. This model was first validated by comparing the experimental and simulated results corresponding to Case A and excellent agreement was achieved (Table 1). It is noted that this

23

model includes the splice losses (estimated theoretically) present on account of fiber mismatches on either side of the YDF, but the background loss is neglected on account of its insignificant value. The code used for this application can be found in the Appendix .
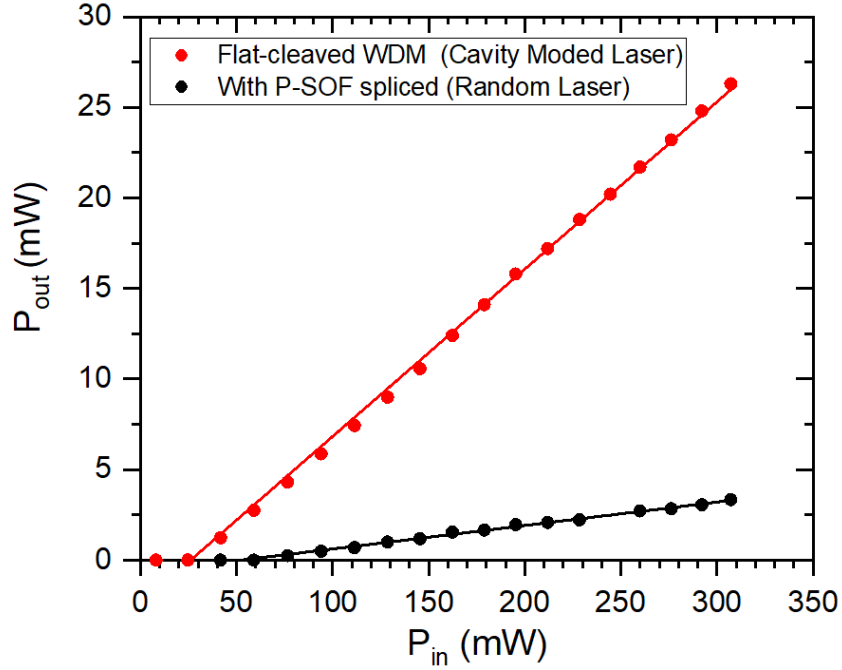

Fig. 17. Output power vs. input power plot for both cases (a) without P-SOF but instead with a flat-cleaved WDM (cavity laser) [Case A], (b) with P-SOF spliced to the WDM (random laser) [Case B].
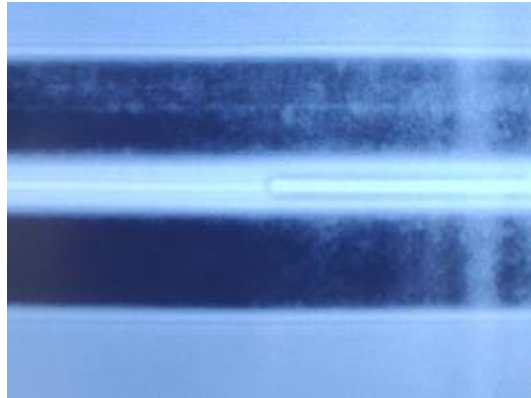

Fig. 18. Detector saturation at the splicer after the splice point (white patches on the dark background - strongly scattered light).

Next, given the slope efficiency and P_{th} obtained from the random laser power curve, an effective power reflectivity (R_{eff}) can be assigned to the scattering fiber. R_{eff} is defined to be the equivalent reflectivity of a conventional reflector that results in the same lasing characteristics as those (P_{th} and η) of the random laser. Its value was adjusted until the model matched experimental results ($\delta(P_{th}) < 6$ mW, $\delta(\eta) <$

0.25%), giving rise to a value of 0.054%. The simulated and experimentally observed values of threshold and slope efficiency for both cases are provided in Table 1. The obtained value for P-SOF reflectivity explains the experimental data obtained very well. Extrapolating from backscattering measurements found in [19] at 1550 nm, the estimated backreflectance at 1050 nm is in reasonable agreement with that obtained from the laser simulation. This is greater than the Fresnel reflectivity of the interface between the connecting fiber and the P-SOF (estimated to be ~0.03%), indicating that distributed reflective feedback from the scattering fiber has a lower lasing threshold than the Fresnel reflection. This computation also provides a metric to model and design a more efficient lasing system since, based on the R_{eff} computed, the reflectivity of the FBG could be optimized for better performance.

Table 1: Laser model performance (comparison with experimental data)

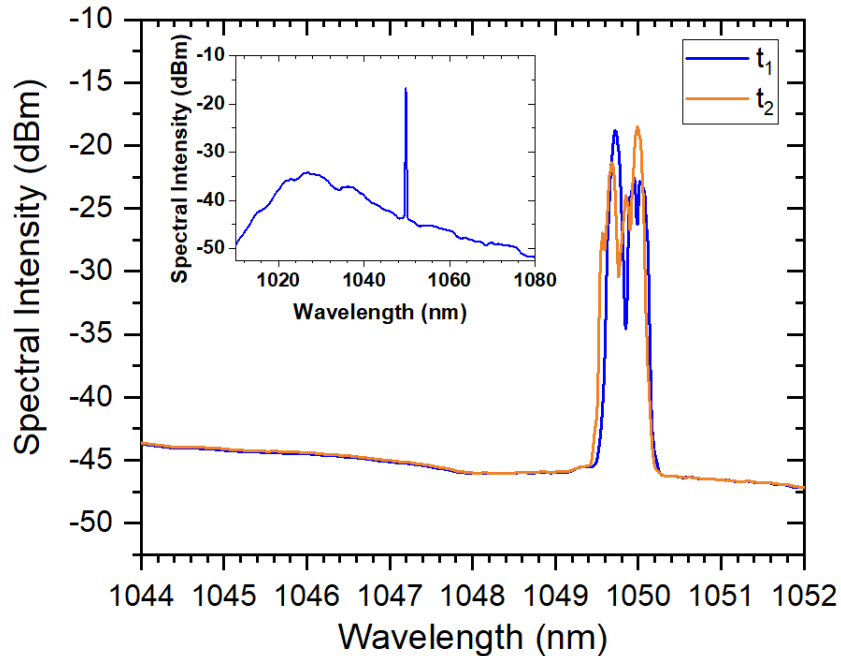| Parameter	Cavity-Mode Laser		Random Laser	
	Experimental	Simulation	Experimental	Simulation
P_{th} (mW)	31.475	39.271	62.1	67.557
η (%)	9.506	9.381	1.307	1.308
Reflectivity values	R1(FBG) – 50.68% R2(Fresnel) – 3.4%		R1(FBG) – 50.68% R2(P-SOF) – 0.054%	

Fig. 19. Laser spectra (single acquisition, non-averaged) at two different instances in time, t_1 and t_2, both spectra taken with P_{in}= 129 mW. (Inset Figure: Broadband spectrum of random laser for same P_{in}.)

Any random spatial sequence of distributed reflectors, in this case in the P-SOF, in terms of the Fourier representation can be thought of as a sum of many very weak regular gratings (randomly distributed) with fixed periods [16]. Extending this analogy, the overall laser multifrequency output then can be

25

thought of as an aggregation of many monochromatic lasers with arbitrary phase and amplitude. The weak nature of the random gratings indicates that the mode structure in the output spectrum would be dominated by the threshold in each of these individual lasers, rather than the gratings themselves. Fig. 19 shows the characteristic temporally dynamic activity in the output spectrum for the random laser, which was observed across the entire range of input powers available. This temporal instability is due to the competition of the lasing modes/frequency components that are formed between the FBG and the randomly distributed reflectors. Although presently constrained in terms of pump power (maximum input power ~ 308 mW), published reports suggest the possibility of temporally stable operation at very high input pump powers [16,40,41]. Fig. 19 also provides a visual understanding of the ASE contribution (inset figure gives the full broadband spectrum of the laser).

Next, the variation of the random laser linewidth with input power is explored. As is clearly apparent, there is spectral broadening with increasing input power (shown in Fig. 20). Since there also is temporal variation (see Fig. 19), these spectra were averaged 25 times. The observed spectral broadening can be attributed to the greater number of wavelength components rising above threshold. We use the term *wavelength components* since the conventional concept of cavity modes does not apply in this case. Essentially, the lasing system can choose from a greater pool of wavelength components that can possibly lase (rise above threshold), and in a random laser, this leads to averaged spectral broadening.
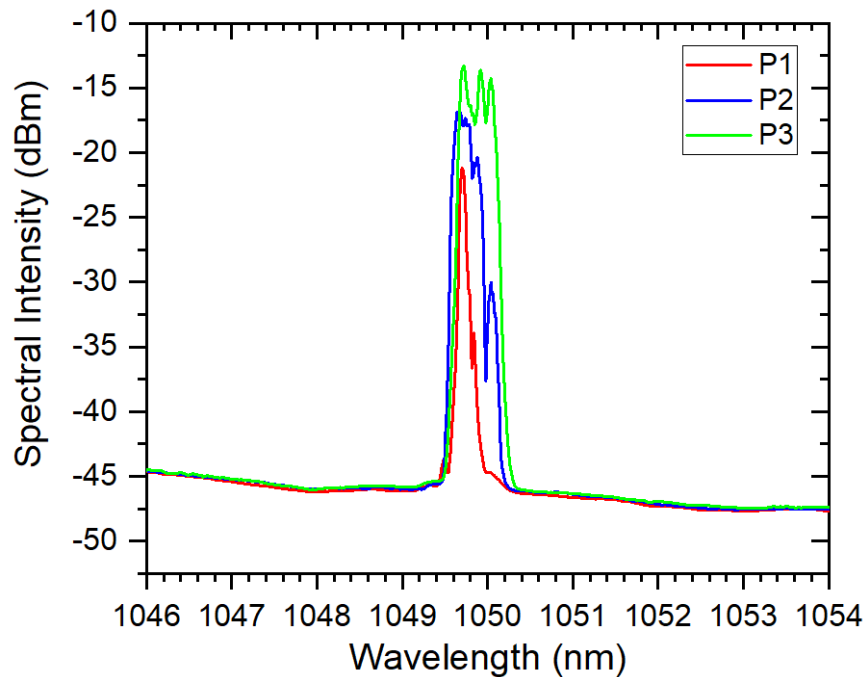

Fig. 20. Averaged output spectra (25 acquisitions) at different input powers, P_1=111 mW, P_2= 212 mW, and P_3= 307 mW.

4.3 RF beat spectra measurements

In order to further verify that the configuration was truly operating in a random state, the RF beat spectra at the output of the laser for both the case with P-SOF spliced onto the WDM (Case B) and flat-cleaved WDM case (Case A) were analyzed. This was done by connecting the laser output to a Si avalanche photodetector and viewing the resulting spectra on an electrical spectrum analyzer to observe any beating between cavity modes, should they exist. Random lasing is associated with a distinct lack of well-defined cavity modes whereas a conventional laser can have many close, equally spaced cavity modes [31,41]. Fig. 21 shows the comparison between both cases and it can clearly be seen that the beating between cavity modes are suppressed in the random laser (Case B) whereas in the cavity-mode case (Case A), a number of cavity modes exist with a spacing very close to the estimated free spectral range (Fabry-Pérot cavity) of about 16 MHz. Essentially, the random laser (Case B) has a "modeless" spectrum consisting of random frequency components. It should be noted that ASE was not removed from the signal in acquiring the data shown in Fig. 21. ASE is a broad continuum and any associated beat noise will have a small power spectral density, and therefore negligible impact on the measurements over a 1 GHz range. The suppression of cavity-mode beating is clear evidence that the lasing is due to feedback from the 3-D array of scatterers rather than from any facet or splice point.
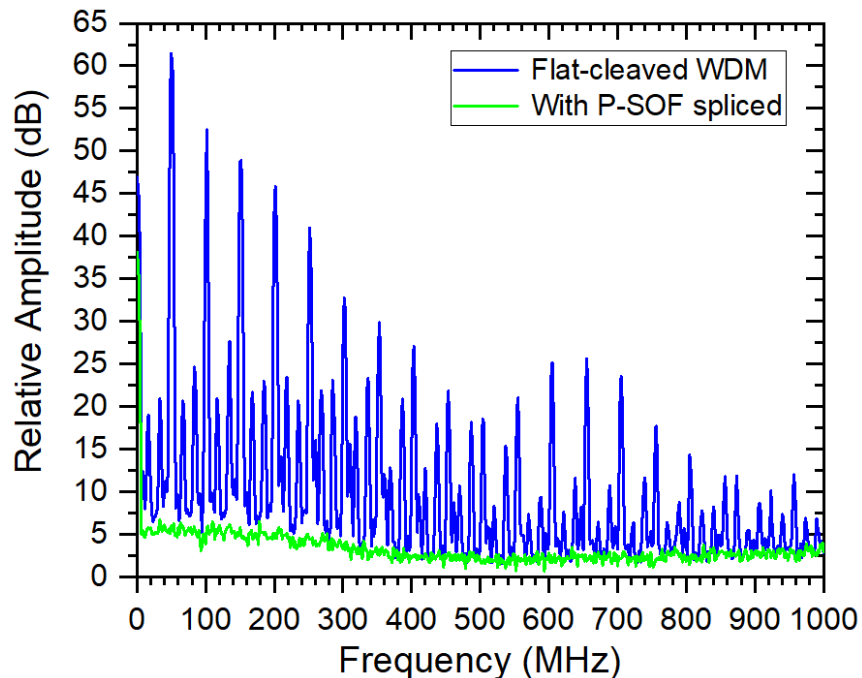

Fig. 21. RF beat spectra taken at P_{out}=1.25 mW for the laser without the P-SOF (WDM flat-cleaved, blue) and with the spliced P-SOF (green) [100 acquisitions averaged].

4.4 Statistics of spectral intensity fluctuations

While the RF beat spectra provide evidence in support of random lasing, more recently the statistical behavior of intensity fluctuations, i.e., the deviation from pre-lasing Gaussian to Lévy-like statistics around the onset of random lasing [42-45], has been established as characteristic behavior expected from a random laser. This phenomenon has been observed in random fiber lasers based on randomized Bragg gratings [43], more recently in a random laser based on Rayleigh feedback with the Raman effect as the gain mechanism [44], and even in plasmonic random lasers [45]. In Section 4.2, temporal spectral variation was discussed; however, here the spectral intensity/power fluctuations are quantified and studied using time domain measurements to garner further evidence in support of the notion that this setup is randomly lasing. This is done by collecting spectral intensity values at different instants of time at a particular wavelength from the Yokogawa AQ6370D Optical Spectrum analyzer using the 0 nm bandwidth setting. The wavelength chosen in this case was 1049.6 nm, well within the lasing spectrum at all input powers, and a spectral resolution of 0.1 nm was used. The histograms of the spectral intensity values generated (about 6000 points) by the spectrum analyzer were then fitted to Lévy α-stable distributions (four parameters [42]) to ascertain the value of the Lévy exponent α.
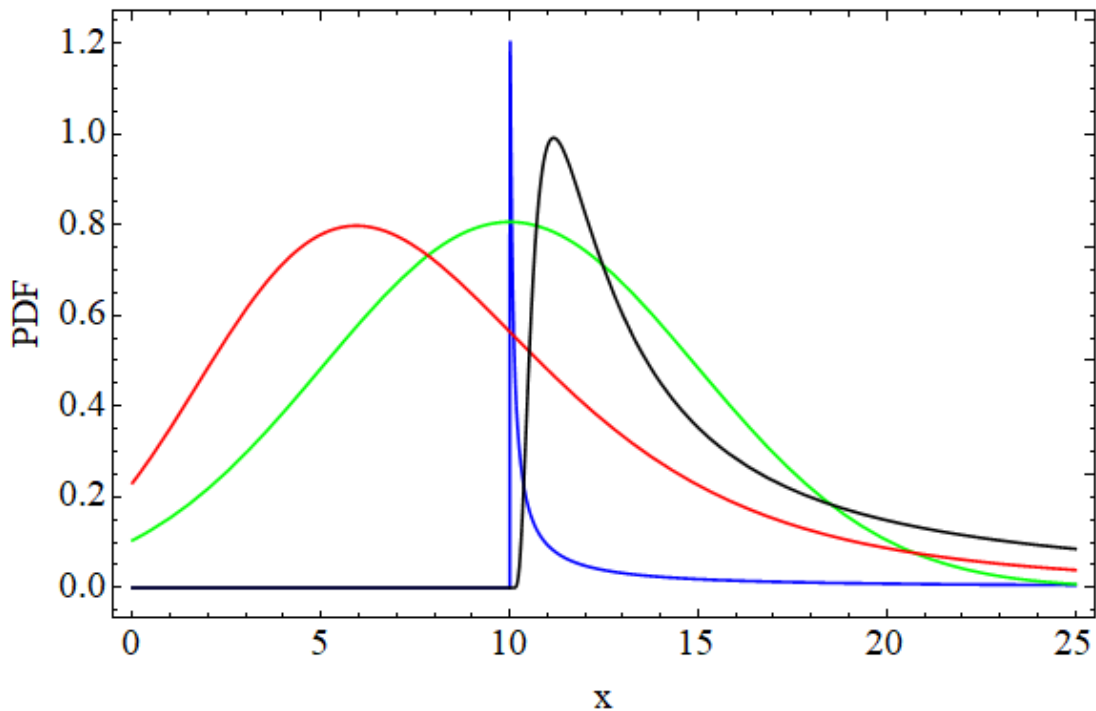

Fig. 22. Vertically scaled Lévy α-stable distribution PDFs plotted for different values of α with all other parameters kept constant [(β, μ, σ)=(1,10,3.5)]; α =0.25 (blue), α=0.5 (black), α=1.5 (red), α=2 (green).

The Lévy α-stable distribution refers to a family of distributions that are stable. A stable distribution is one which satisfies the following condition: a linear combination of two independent random variables with this distribution has the same distribution. There are multiple parameterizations for stable laws; however, the four-parameter parametrization with the associated notation $S(\alpha, \beta, \sigma, \mu)$ is typically used as the standard parametrization. The four parameters associated with the Lévy α-stable distribution are α which is the index of stability/characteristic exponent (determines the type of distribution and distribution characteristics), β which is the skew parameter (determines symmetricity and the direction of the tail), μ which is the location parameter (analogous to mean, controls lateral movement of the distribution) and σ which is the scale parameter (analogous to standard deviation, controls the spread). It is noted that a generalized PDF (probability density function) for the Lévy α-stable distribution cannot be analytically represented using a closed form expression. However, distributions that have closed form expressions like the Cauchy distribution ($S(1,0,\gamma,\delta)$) are also part of the Lévy α-stable distribution family. Due to the lack of a general closed form expression, the α-stable distribution is conveniently described by the characteristic function $\phi(t)$, i.e. the inverse Fourier transform of the PDF. The expressions for $\phi(t)$ in terms of the four parameters $\alpha, \beta, \sigma, \mu$ are given below [42]:

$$ln\big(\phi(t)\big) = -\sigma^\alpha|t|^\alpha\left\{1 - i\beta sgn(t)\,tan\left(\frac{\pi\alpha}{2}\right)\right\} + i\mu t \qquad \alpha \neq 1 \qquad (4.1)$$

$$ln\big(\phi(t)\big) = -\sigma|t|\left\{1 - i\beta sgn(t)\left(\frac{\pi}{2}\right)^{-1}\right\} + i\mu t \qquad\qquad \alpha = 1 \qquad (4.2)$$

where $sgn(t)$ refers to the signum function and i is the unit imaginary number. In Eq. (4.1) and Eq. (4.2), the Lévy index $\alpha \in (0,2]$ is the most important parameter, since it drives the type of statistics that characterize the fluctuations of the random variables. While strong fluctuations with relevant deviations from the Gaussian behavior are associated with values in the range $0 < \alpha < 2$, the Gaussian statistics with weak fluctuations are recovered for the boundary value $\alpha = 2$. Essentially, an α value of 2 corresponds to a Gaussian distribution whereas an α value less than 2 corresponds to the Lévy statistical regime. Fig. 22 shows the PDF plots for different values of α while keeping the remaining parameters constant. The PDFs for different α values are vertically scaled in order to visually represent the shapes of the distributions better.

Based on the spectral intensity data obtained from the optical spectrum analyzer measurements, the PDF of intensity values for each value of normalized pump power is generated and fitted to the Lévy α-stable distribution to ascertain α. The variation of α with normalized input power (as a fraction of the threshold power) is shown in Fig. 23. It is noted that since the pump is temperature stabilized, the pump

power variations are negligible and the spectral intensity fluctuations stem mainly from laser behavior. Three statistical regimes of spectral intensity/power fluctuations are observed for the RFL system: pre-lasing Gaussian (α = 2), Lévy statistics (0 < α <2) around the threshold, and Gaussian statistics (α =2) well above the threshold (P_{in}/P_{th} >2.7). Below threshold, the output is basically ASE which has Gaussian statistics in terms of intensity fluctuations. However, close to threshold, a given mode can dominate over the others, siphoning off all the gain. In this case, large fluctuations in the output intensities related to the dominating modes can result from relevant fluctuations in the respective path lengths of the diffusing photons. Thus, the possibility of extreme events increases, and this leads to the long tailed Lévy distribution. However, as the normalized input power increases, the distribution of the gain among the active modes becomes more and more homogeneous, diminishing considerably the probabilities of extreme events of intensity and rather long diffusing paths, essentially leading to a Gaussian distribution [43]. The observation of three distinct statistical regimes and a sharp drop-off in α at the threshold power is consistent with the trends observed in previous works employing fiber based random lasers [43,44], indicating that the fiber lasing setup is randomly lasing.
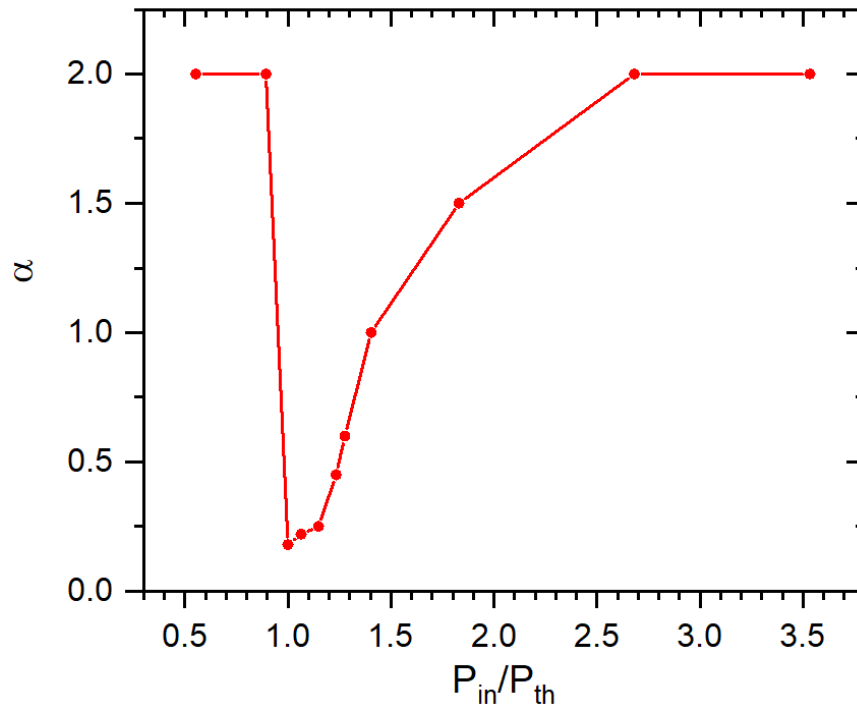

Fig. 23. Variation of the Lévy exponent α with the normalized input power (normalized to the threshold power).

4.5 Coherence measurements

The coherence of the random laser was investigated using Young's double slit experiment [46]. The commercially available, vertical double slit (3B Scientific Corporation, USA) had a slit width of 0.15 mm

and a slit spacing of 1 mm. The laser output was collimated to a diameter that illuminated both slits symmetrically. The resulting fringes were recorded at a distance of approximately 37 cm from the slits with a CMOS machine vision camera. A neutral-density filter was used to prevent saturation when required. First, a central image was obtained for both cases, as shown in Fig. 24. Then, the camera was translated in the transverse direction (parallel to the plane of the slits) to record the fringe visibility as a function of distance from the central position. The resulting extended fringe pattern shown in Fig. 25 was generated by stitching together those images at different positions, thereby inducing a few discontinuities. Note also that the central fringe in Fig. 25 has an almost constant intensity value due to saturation of the camera. This is on account of the higher power required to observe weaker higher fringe orders, accomplished by decreasing the optical attenuation.

Finally, to quantitatively and qualitatively evaluate the degree of coherence, the mutual coherence function (γ) is obtained from the fringe data. In this measurement, the intensity on both slits is assumed to be equal and γ reduces to the fringe visibility (V) given by [47]:

$$V = \frac{I_{max} - I_{min}}{I_{max} + I_{min}} \tag{4.3}$$

where I_{max} and I_{min} are the maximum and minimum intensities of the interference fringes, respectively.

The results shown in Fig. 24 confirm that the random laser is spatially coherent, just as is observed with the cavity-mode laser (Case A), since clearly defined fringes are exhibited. This can be explained by the fact that the transverse mode is constrained to the fundamental since the YDF, WDM fiber, and the connecting fiber are all single-mode at 1050 nm. Though many spatial modes may be excited by scattering in the P-SOF, only the random frequency components corresponding to the fundamental spatial mode can couple back efficiently into the system. These components experience gain and concurrently can lase. Essentially, this configuration does not allow for random behavior to manifest in the transverse spatial dimension. However, a legitimate comparison of the degree of spatial coherence can be made by considering the visibility of only the central fringe. This was found to be 0.68 and 0.74 for the random and cavity-mode lasers, respectively, at equivalent output powers of 1.6 mW. The central fringe visibility was found to be slightly less in the case of the random laser possibly due to the greater ASE observed. However, it is noted that the central fringe visibility is relatively high in both cases, which is characteristic of a spatially coherent laser source [46].
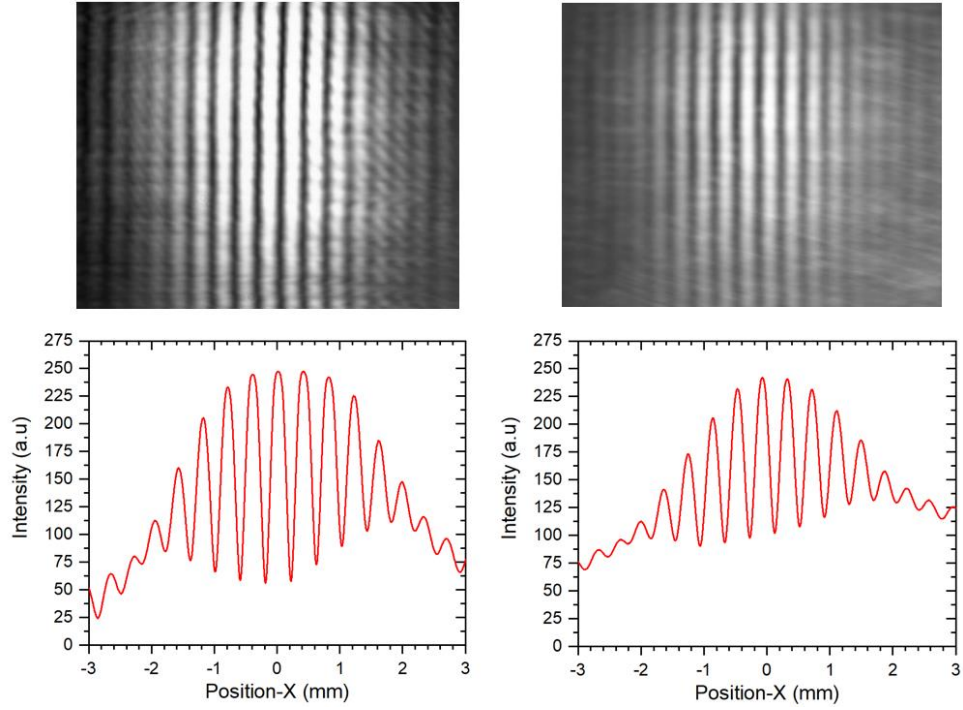
Fig. 24. Interference fringes observed from the outputs of the [left] cavity-mode laser and the [right] random laser (Top: fringe pattern camera image; Bottom: spatially averaged fringe data) [P_{out} ~ 1.6 mW].
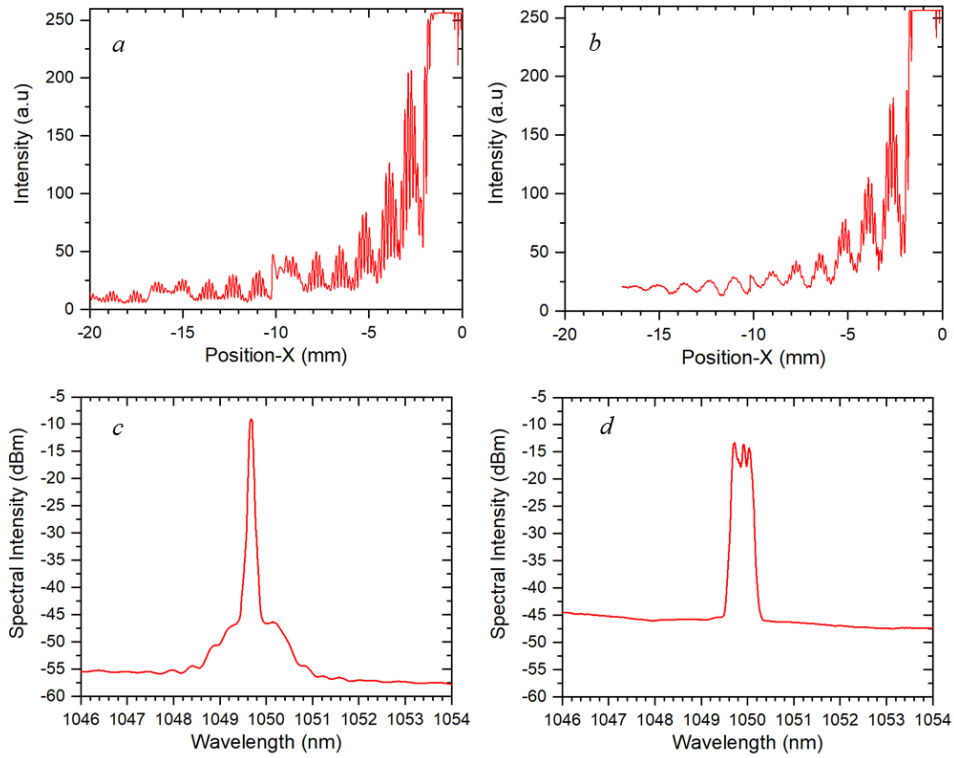

Fig. 25. Spatially averaged fringe pattern intensity (0-255) as a function of horizontal position (x) for (a) cavity-mode laser (without P-SOF) and (b) random laser (with P-SOF). Corresponding spectra for (c) cavity-mode laser and (d) random laser (P_{out} ~ 3.3 mW).

32

In Fig. 25, only select fringe orders, or rather fringe groupings, are visible. The sinc^2 spatial envelope function is a consequence of the finite slit width used, as opposed to the ideal scenario (infinitesimal slit width) where every order would be visible. Decay of the fringe visibility with the fringe order is observed, with the random laser exhibiting fewer distinguishable fringe groups and a faster decay of fringe visibility (depth of modulation of the fringe patterns). This observation is fully in line with its broader linewidth, which necessarily implies a lower coherence length (temporal coherence). The output power was maintained the same for both cases (~ 3.3 mW) in order to standardize the comparison.

4.6 Cut-back experiments

In order to study the impact of P-SOF length on lasing characteristics, cut-back experiments were performed. In particular, the RF beat spectra were recorded as a function of P-SOF length. In the first study, a flat-cleave at the end of the P-SOF provides additional reflective feedback (Fresnel reflection) from the fiber-to-air interface. From Fig. 26, as the length of the P-SOF decreases, more peaks with larger amplitudes begin to appear in the RF beat spectra, indicating the presence of a greater number of stronger cavity modes. This signifies that the relative strength of the reflective (Fresnel) feedback increases with decreasing P-SOF length (Rayleigh feedback decreases, Fresnel feedback increases), consequently increasing the number and strength of cavity modes. As a side note, it also was observed (but not shown here) that the number of peaks increases with increasing input pump power. This is to be expected, as more cavity modes surpass the threshold. Observed temporal instability in the amplitude and position of these peaks in the spectra indicates competition between different cavity modes for dominance. At very short P-SOF lengths, the RF beat spectra begin resembling a purely cavity-mode laser, also as expected, since now the Fresnel reflection completely dominates over the severely reduced distributed Rayleigh feedback. The threshold powers however did not change significantly across the experiment.

A second cut-back experiment was performed, this time with an angled cleave (20°) at the P-SOF fiber end in order to remove the effects of feedback due to Fresnel reflection. The laser behavior is random across the entire range P-SOF fiber lengths evaluated and input pump powers over threshold, as is evidenced by the fact that the RF beat spectra possess no peaks corresponding to cavity-mode beating. By way of example, Fig. 27 shows the RF beat spectra for a P-SOF length of 1.5 m at two different input powers (and cleaved at an angle). The other observation here (Fig. 27, inset figure) is that the threshold power increases as the length decreases (though the P_{th} becomes asymptotic at lower lengths). This is

further evidence supporting random lasing from the phase separated fiber, since as R_{eff} decreases the threshold increases.
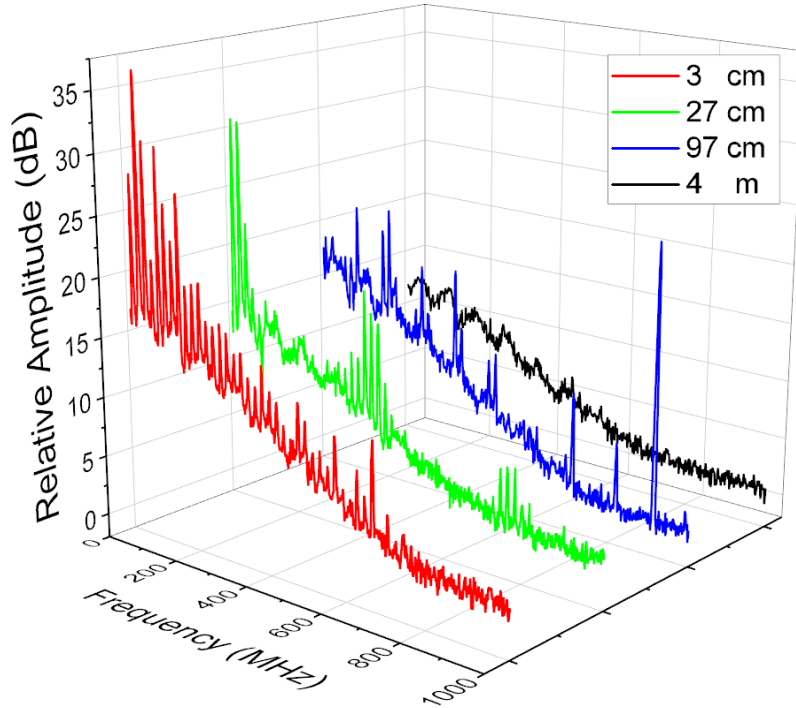

Fig. 26. RF beat spectra (10 MHz- 1 GHz) at P_{in} = 307 mW for different cutback lengths (with Fresnel reflection concatenated, legend indicates length of P-SOF spliced) [100 acquisitions averaged].
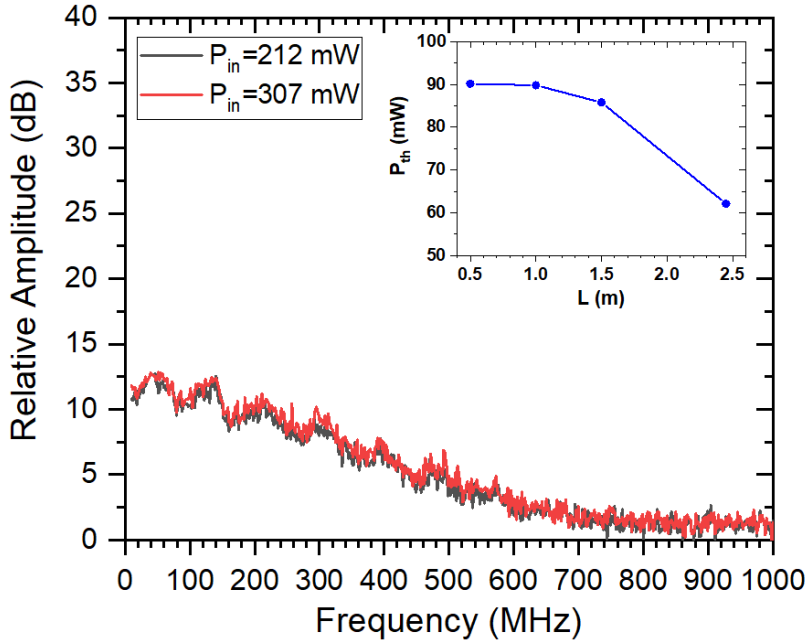

Fig. 27. RF beat spectra (10 MHz – 1 GHz) at different input powers for spliced P-SOF length of 1.5 m (angled cleave at fiber end) [100 acquisitions averaged]. (Inset Figure: P_{th} vs. length of angle cleaved P-SOF spliced onto the system.)

To conclude, it is also noted that a length of 2.45 m is the minimum length of the fabricated P-SOF required for efficient random lasing. This length was identified empirically to be the point where laser threshold and concomitant increase in the light emerging from the angled-cleaved facet (scattering fiber side), and at the same time the P-SOF length, are all minimized. In other words, longer P-SOF fiber lengths did not lead to any further reduction in P_{th}.

5. Possible Applications and Future Work

While random fiber lasers are an up-and-coming field with research still in progress to find novel applications, there have been demonstrations of random laser based applications [3,48] where the proposed design definitely could be of use. In Ref. [3], a random fiber laser based on Rayleigh scattering is used for speckle-free imaging. In this case, a large length of highly multimode fiber is used after the single transverse-mode random fiber laser to excite higher order modes. This would lead to the reduction in speckle contrast (C = 1/ √m, where m is the number of modes). This reduction in speckle contrast coupled with the high spectral density of the RFL allows for better imaging than even multimode ASE sources. It is also to be noted that in this configuration, the reduced spatial coherence of an RFL and the larger linewidth of its spectrum clearly makes it superior to a conventional single-mode narrow linewidth laser. In Ref. [48], an RFL with internal modulation is shown to have reduced distortion. It is claimed that the flat frequency response of this internally modulated random laser allows for a temporal response with reduced distortion independent of modulation frequency. This is in contrast to conventional internally modulated fiber lasers where the length of the laser cavity distorts the analog internal modulation and determines the repetition rate of generated pulses. In random fiber lasers, the feedback does not correspond to a fixed length, so there is no distortion of the modulating frequency or self-mode-locking effects [48,8].

Possible avenues to be explored include investigations into other glass families (calcium-silicate fiber), high linewidth and high power lasers, and power scaling through the use of a master oscillator power amplifier (MOPA) configuration. With respect to the investigations into other glass families, the use of calcium silicate fibers as the source of random feedback represents an intriguing proposition. The larger particle size (still $<\lambda$) indicates that Mie scattering may also play a role in the overall light scattered. Mie scattering is predominantly forward scattering and its impact on the overall scattering profile is based on the non-dimensional size parameter ($x = 2\pi r/\lambda$) defined based on the particle properties (r -radius of the particle) and the wavelength (λ). If x is comparable to or greater than 1, Mie scattering will begin to dominate, which is the case in the calcium silicate fiber mentioned in Chapter 3 ($x\sim0.8$). It is noted that this formulation provides a rough estimate of scattering characteristics of a spherical particle and is useful in estimating the dominant scattering phenomena; however, non-sphericity and multiple scattering will also impact the actual scattering characteristics. The impact of the enhanced Mie scattering alongside the Rayleigh scattering provides interesting avenues for further research. While the random laser setup described previously shows spectral broadening, the overall linewidth is still limited by the FBG bandwidth. However, if a point-based reflector with approximately wavelength independent

spectral response were to be used (straight cleave based Fresnel feedback), there exists the possibility of very high linewidth realization, though the lasing wavelength would basically be the local maxima of the emission cross section (~1030 nm). Using multimode high-power pumps could definitely boost the input (~W) and corresponding output powers, possibly adding in the additional characteristic of high temporal stability. A schematic of the tentative setup is as shown in Fig. 28.
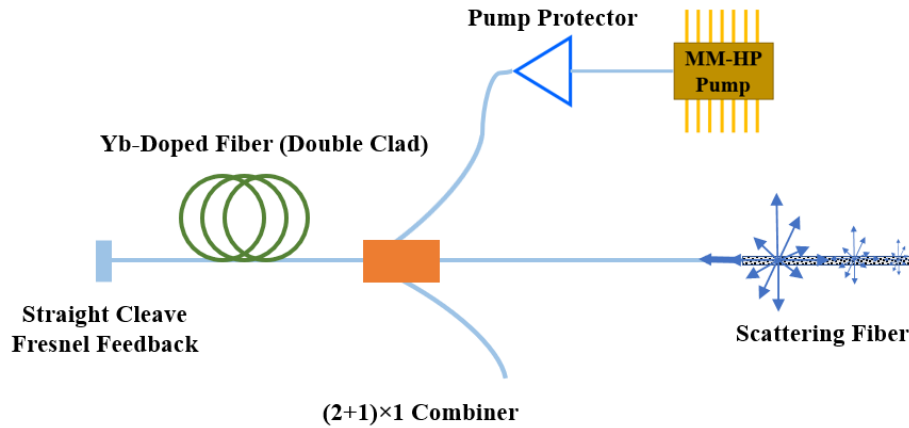

Fig. 28. Proposed setup for high linewidth and high power RFL.

The output power of the setup investigated in this work is still pretty low ($P_{max}^{out} \sim 3.3$ mW). This means that using additional amplifying stage(s) is a good idea. So, one possible setup for this would be a MOPA configuration. However, addition of a pre-amp stage before high power amplification would definitely boost the output while still operating in the small signal range. The characteristics of the amplified laser spectrum would be of tremendous interest (temporal stability, intensity variation etc.). The proposed setup for a MOPA configuration with a pre-amp stage added in is shown in Fig. 29.
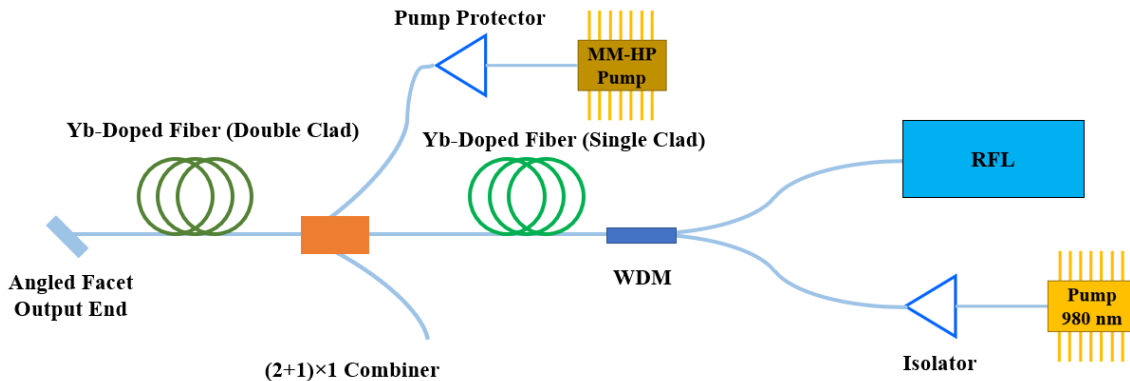

Fig. 29. Proposed setup for MOPA based amplification of random fiber laser spectrum.

37

All these setups and ideas represent attractive prospects in terms of research, and work is already underway to experiment with some or all of the aforementioned setups. However, by no means are these ideas exhaustive; alternate strategies are also under formulation for future work.

6. Conclusion

In conclusion, a novel low threshold random laser at 1050 nm with a maximum output power of 3.3 mW using a phase separated aluminosilicate core – silica cladding fiber (P-SOF) as the reflecting medium has been demonstrated. The P-SOF was fabricated with the molten core method and was found to exhibit nano-scale phase separation and, therefrom, enhanced Rayleigh scattering. Rayleigh scattering was established as the dominant mode of scattering and a new figure of merit for random feedback termed as *effective power reflectivity* was developed. The salient features of this random laser include significantly reduced required P-SOF length rendering an ultra-short cavity setup (approximately a few meters, in contrast to the ~100s of meters to km required when using conventional fiber setups) [15-18,41], laser linewidth and lasing wavelength control through the use of an FBG, output characteristics allowing for conventional YDF-based amplification, and low threshold power. Measurements were made confirming the random lasing action through RF beat spectrum measurements. The random lasing action was also confirmed from the trends in the Lévy exponent α obtained from spectral intensity variation measurements. This random laser was found to have a high degree of spatial coherence, though slightly less than its cavity-mode counterpart, and its temporal coherence was found to be consistent with the linewidth. Cutback experiments were also carried out, shedding light on the evolution of lasing behavior with P-SOF length spliced onto the system and the impact of feedback on the lasing characteristics. The minimum length of P-SOF required for maximum Rayleigh-distributed feedback was also determined to be ~ 2.5 m. The present work establishes this compact random laser configuration. While random fiber lasers based on Rayleigh scattering are an up-and-coming field with research still ongoing to find novel applications, this setup potentially lends itself well to use in speckle-free imaging [3] and internally modulated lasers with reduced distortion [48]. Power scaling efforts and investigations into other glass families are currently ongoing.

References

1. R. V. Ambartsumyan, N. G. Basov, P. G. Kryukov, and V. S. Letokhov, "Non-resonant feedback in lasers," Progress in Quantum Electronics **1**, 107-185 (1970).

2. B. Redding, M. Choma, and H. Cao, "Speckle-free laser imaging using random laser illumination," Nature Photonics **6**(6)**,** 355-359 (2012).

3. R. Ma, Y. J. Rao, W. L. Zhang and B. Hu, "Multimode random fiber laser for speckle-free Imaging," IEEE Journal of Selected Topics in Quantum Electronics **25**(1), 1-6 (2018).

4. Z. N. Wang, Y. J. Rao, H. Wu, P. Y. Li, Y. Jiang, X. H. Jia, and W. L. Zhang, "Long-distance fiber-optic point-sensing systems based on random fiber lasers," Optics Express **20**(16), 17695-17700 (2012).

5. M. Fernandez-Vallejo, M. Bravo and M. López-Amo, "Ultra-long laser systems for remote fiber Bragg gratings arrays interrogation," IEEE Photonics Technology Lett. **25**(14), 1362-1364 (2013).

6. D. S. Wiersma, "The physics and applications of random lasers," Nature Physics **4**(5), 359-367 (2008).

7. X. H. Jia, Y. J. Rao, Z. N. Wang, W. L. Zhang, Y. Jiang, J. M. Zhu, and Z. X. Yang, "Towards fully distributed amplification and high-performance long-range distributed sensing based on random fiber laser," in Proceedings of 22nd International Conference on Optical Fiber Sensor (OFS2012) **8421**, 842127 (2012).

8. D. V. Churkin, S. Sugavanam, I. D. Vatnik, Z. Wang, E. V. Podivilov, S. A. Babin, Y. Rao, and S. K. Turitsyn, "Recent advances in fundamentals and applications of random fiber lasers," Advances in Optics and Photonics **7**(3), 516-569 (2015).

9. Q. Song, S. Xiao, Z. Xu, V. M. Shalaev, and Y. L. Kim, "Random laser spectroscopy for nanoscale perturbation sensing," Optics Letters **35**(15), 2624-2626 (2010).

10. Y. Li, P. Lu, X. Bao, and Z. Ou, "Random spaced index modulation for a narrow linewidth tunable fiber laser with low intensity noise," Optics Letters **39**(8), 2294-2297 (2014).

11. M. Gagné, and R. Kashyap, "Demonstration of a 3 mW threshold Er-doped random fiber laser based on a unique fiber Bragg grating," Optics Express **17**(21), 19067-19074 (2009).

12. W. L. Zhang, R. Ma, C. H. Tang, Y. J. Rao, X. P. Zeng, Z. J. Yang, Z. N. Wang, Y. Gong, and Y. S. Wang, "All optical mode controllable Er-doped random fiber laser with distributed Bragg gratings," Optics Letters **40**(13), 3181-3184 (2015).

13. X. Wang, D. Chen, H. Li, L. She, and Q. Wu, "Random fiber laser based on artificially controlled backscattering fibers," Applied Optics **57**(2), 258-262 (2018).

14. S. Sebastian, C. L. Linslal, C. P. G. Vallabhan, V. P. N. Nampoori, P. Radhakrishnan, and M. Kailasnath, "Random lasing with enhanced photostability of silver nanoparticle doped polymer optical fiber laser," Laser Physics Letters **11**(5), 055108 (2014).

15. H. Zhang, P. Zhou, H. Xiao and X. Xu., **"**Efficient Raman fiber laser based on random Rayleigh distributed feedback with record high power," Laser Physics Letters **11** (7), 075104 (2014).

16. S. K. Turitsyn, S. A. Babin, A. E. El-Taher, P. Harper, D. V. Churkin, S. I. Kablukov, J. D. Ania-Castañón, V. Karalekas, and E. V. Podivilov, "Random distributed feedback fibre laser," Nature Photonics **4**(4), 231 (2010).

17. Q. Meng, H. Wu, B. Han, J. Li, and Z. Wang, "LD-pumped random fiber laser based on erbium-ytterbium Co-doped fiber," Photonic Sensors 1-5 (2019).

18. H. Zhang, H. Xiao, P. Zhou, X. Wang, and X. Xu, "Random distributed feedback Raman fiber laser with short cavity and its temporal properties," IEEE Photonics Technology Letters **26**(16), 1605-1608 (2014).

19. M. Cavillon, P. Dragic, B. Greenberg, S. H. Garofalini, and J. Ballato, "Observation and practical implications of nano-scale phase separation in aluminosilicate glass optical fibers," Journal of the American Ceramic Society **102**(3), 879-883 (2019).

20. J. Ballato and A. C. Peacock, "Perspective: Molten core optical fiber fabrication- A route to new materials and applications," APL Photonics **3**(12), 120903 (2018).

21. S. Jagannathan, L. Ackerman, W. Chen, N. Yu, M. Cavillon, M. Tuggle, T.W. Hawkins, J. Ballato, and P.D. Dragic, "Random lasing from optical fibers with phase separated glass cores," Optics Express **28**(15), 22049-22063 (2020).

22. B.E. Saleh and M.C. Teich, Fundamentals of Photonics, John Wiley & Sons (2019).

23. J. E. Midwinter, Optical Fibers for Transmission, Wiley, 1979.

24. The guided modes of an optical fiber, web page. Available at: http://www.joy-david-alex-vincent.co.uk/fibremodes.htm Accessed July 2020.

25. M. Nakazawa, "Rayleigh backscattering theory for single-mode optical fibers," JOSA, **73**(9), 1175-1180 (1983).

26. K. Tsujikawa, K. Tajima, and M. Ohashi, "Rayleigh scattering reduction method for silica-based optical fiber," Journal of Lightwave Technology, **18**(11), 1528 (2000).

27. Corning SMF 28 Optical Fiber, datasheet, Corning, Inc., 2002. Available at: https://mathscinotes.com/wp-content/uploads/2017/03/corning-smf-28.pdf

28. A. Bucholtz, "Rayleigh-scattering calculations for the terrestrial atmosphere," Applied Optics **34**(15), 2765-2773 (1995).

29. J. Xie, S. Mita, Z. Bryan, W. Guo, L. Hussey, B. Moody, R. Schlesser, R. Kirste, M. Gerhold, R. Collazo, and Z. Sitar, "Lasing and longitudinal cavity modes in photo-pumped deep ultraviolet AlGaN heterostructures," Applied Physics Letters, **102**(17), 171102 (2013).

30. T. Zhai, X. Zhang, Z. Pang, X. Su, H. Liu, S. Feng, and L. Wang, "Random laser based on waveguided plasmonic gain channels," Nano letters, **11**(10), 4295-4298 (2011).

31. S.K. Turitsyn, S.A. Babin, D.V. Churkin, I.D. Vatnik, M. Nikulin, and E.V. Podivilov, "Random distributed feedback fibre lasers," Physics Reports, **542**(2), pp.133-193 (2014).

32. S.A. Babin, V. Karalekas, E.V. Podivilov, V.K. Mezentsev, P. Harper, J.D. Ania-Castañón, and S.K. Turitsyn, "Turbulent broadening of optical spectra in ultralong Raman fiber lasers," Physical Review A, **77**(3), 033803 (2008).

33. F. Auzel, and P. Goldner, "Towards rare-earth clustering control in doped glasses," Optical Materials, **16**(1-2), 93-103 (2001).

34. P.D. Dragic, M. Cavillon, and J. Ballato, "Materials for optical fiber lasers: A review," Applied Physics Reviews, **5**(4), 041301 (2018).

35. M.N. Zervas, and C.A. Codemard, "High power fiber lasers: A review," IEEE Journal of Selected Topics in Quantum Electronics, **20**(5), pp.219-241 (2014).

36. A.K. Varshneya, Fundamentals of Inorganic Glasses, Elsevier (2013).

37. K.C. Kao and G.A. Hockham, "Dielectric-fibre surface waveguides for optical frequencies," in Proceedings of the Institution of Electrical Engineers **113**(7), 1151-1158 (1966).

38. A. D. Yablon, "Multi-wavelength optical fiber refractive index profiling by spatially resolved Fourier transform spectroscopy," Journal of Lightwave Technology **28**(4), 360–364 (2009).

39. C. Barnard, P. Myslinski, J. Chrostowski, and M. Kavehrad, "Analytical model for rare-earth-doped fiber amplifiers and lasers," in IEEE Journal of Quantum Electronics **30**(8), 1817-1830 (1994).

40. A. A. Fotiadi, "Random lasers: An incoherent fibre laser," Nature Photonics **4**(4), 204–205 (2010).

41. S. A. Babin, A. E. El-Taher, P. Harper, E. V. Podivilov, and S. K. Turitsyn, "Tunable random fiber laser," Physical Review A **84**(2), 021805 (2011).

42. R. Uppu, and S. Mujumdar, "Lévy exponents as universal identifiers of threshold and criticality in random lasers," Physical Review A **90**(2), 025801 (2014).

43. B.C. Lima, A.S. Gomes, P.I. Pincheira, A.L. Moura, M. Gagné, E.P. Raposo, C.B. de Araújo, and R. Kashyap, "Observation of Lévy statistics in one-dimensional erbium-based random fiber laser," JOSA B **34**(2), 293-299 (2017).

44. J. Li, H. Wu, Z. Wang, S. Lin, C. Lu, E.P. Raposo, A.S. Gomes, and Y. Rao, "Lévy spectral intensity statistics in a Raman random fiber laser," Optics Letters **44**(11), 2799-2802 (2019).

45. J.H. Hsiao, S.W. Chen, B.Y. Hung, K. Uma, W.C. Chen, C.C. Kuo, and J.H. Lin, "Resonant energy transfer and light scattering enhancement of plasmonic random lasers embedded with silver nanoplates," RSC Advances, **10**(13), 7551-7558 (2020).

46. Y. Deng, D. Chu, "Coherence properties of different light sources and their effect on the image sharpness and speckle of holographic displays," Sci Rep **7**(1), 1-12 (2017).

47. B. Redding, M. A. Choma, and H. Cao, "Spatial coherence of random laser emission," Optics Letters **36**(17), 3404-3406 (2011).

48. M. Bravo, M. Fernandez-Vallejo, and M. Lopez-Amo, "Internal modulation of a random fiber laser," Optics Letters **38**(9),1542-1544 (2013).

Appendix: Laser Model Code

Red text indicates user-entered inputs (lifetime, cross-sections, reflectivities, etc.). Blue text provides context and additional information as required, and also headlines the different sections. It is noted that output appears through the R2 end (FBG reflectivity of 50.68%) and R1 is varied accordingly. As discussed in Chapter 4, initially the model is run with parameters corresponding to cavity-mode laser; thereafter, R1 is varied in order to obtain the effective power reflectivity for the random laser case.

 (* Note here that an index of 1 in a variable name implies pump wavelength and that a 2 implies the seed wavelength. *)

(* Assume LP(lm)=LP(01) mode so that l=0 *)

ClearAll[FiberLength,Eps,Eps1,Eps2,Eps1P];

l = 0;

(* Wavelengths, Numerical Aperture, Core Diameter, in meters *)

(* The text in green is for an elliptical core.

  It gives an effective radius for a circular fiber. *)

a = 1 * 10^-6;
b = 2 * 10^-6;
DcoreEff = N[2*Sqrt[a*b]];

Lambda1 = 976 * 10^-9; (* Pumping Wavelength *)
Lambda2 = 1050 * 10^-9; (* Lasing Wavelength *)
Lambda3 = 1530 * 10^-9;   (* ASE Wavelength, can be ignored*)
NA = 0.2;   (* Insert the NA*)
Dcore = 4.1 * 10^-6;   (* Core diameter*)

(* Fiber 'V' constants *)

V1 = Pi * Dcore * NA / Lambda1//N
V2 = Pi * Dcore * NA / Lambda2//N
V3 = Pi * Dcore * NA / Lambda3//N

(* Calculate the modes *)

(* Seed modal structure next *)

Y1 = Sqrt[(V1)^2 - (X1)^2];
pumpa = (X1)BesselJ[1,X1]/BesselJ[0,X1];
pumpb = (Y1)BesselK[1,Y1]/BesselK[0,Y1];
Plot[{pumpa,pumpb},{X1,0,V1}];

44

Xpump=FindRoot[pumpa-pumpb==0,{X1,1.6}]

(* Seed modal structure *)

Y2 = Sqrt[(V2)^2 - (X2)^2];
seeda = (X2)BesselJ[1,X2]/BesselJ[0,X2];
seedb = (Y2)BesselK[1,Y2]/BesselK[0,Y2];
Plot[{seeda,seedb},{X2,0,V2}];
Xseed=FindRoot[seeda-seedb==0,{X2,1.6}]

(*Roots of the dispersion relation used to
   define the modal wavenumbers. *)
IntersectX1 = X1/.Xpump;
IntersectX2 = X2/.Xseed;
IntersectX3 = X3/.Xase;
IntersectY1 = Sqrt[(V1)^2 - (IntersectX1)^2];
IntersectY2 = Sqrt[(V2)^2 - (IntersectX2)^2];
IntersectY3 = Sqrt[(V3)^2 - (IntersectX3)^2];

(* Modal Wavenumber given in inverse microns. *)
Kt1 = IntersectX1/(.5*Dcore)/10^6;
Kt2 = IntersectX2/(.5*Dcore)/10^6;
Kt3 = IntersectX3/(.5*Dcore)/10^6;
Gam1 = IntersectY1/(.5*Dcore)/10^6;
Gam2 = IntersectY2/(.5*Dcore)/10^6;
Gam3 = IntersectY3/(.5*Dcore)/10^6;

(*Core mode structure *)
Mode1Core=Plot[(BesselJ[0,Kt1*r])^2,{r,0,(10^6)*Dcore/2}];

(* Cladding mode structure with matched boundary condition *)
BoundaryCondition1 = BesselJ[0,Kt1*(10^6)*Dcore/2]/
             BesselK[0,Gam1*(10^6)*Dcore/2];

Mode1Clad=Plot[(BoundaryCondition1)^2
          (BesselK[0,Gam1*r])^2,{r,(10^6)*Dcore/2,(10^6)*Dcore}];

(* Total pump mode picture *)
aaa = Show[Mode1Core,Mode1Clad,PlotRange->All];

(* Electric field equations for future use *)
ClearAll[CoreMode1,CoreMode2];
CoreMode1 = BesselJ[0,Kt1*r];
CladMode1 = (BoundaryCondition1)*BesselK[0,Gam1*r];

(* Seed mode *)

(* Core mode structure *)

Mode2Core=Plot[(BesselJ[0,Kt2*r])^2,{r,0,(10^6)*Dcore/2},PlotRange->All];

(* Cladding mode structure with matched boundary condition *)

BoundaryCondition2 = BesselJ[0,Kt2*(10^6)*Dcore/2]/BesselK[0,Gam2*(10^6)*Dcore/2];

Mode2Clad=Plot[(BoundaryCondition2)^2
(BesselK[0,Gam2*r])^2,{r,(10^6)*Dcore/2,(10^6)*Dcore},PlotRange->All];

(* Total seed mode picture *)
bbb = Show[Mode2Core,Mode2Clad,PlotRange->All];

Show[aaa,bbb]

(* Electric field equations for future use *)
CoreMode2 = BesselJ[0,Kt2*r];
CladMode2 = (BoundaryCondition2)BesselK[0,Gam2*r];

Mode3Core=Plot[(BesselJ[0,Kt3*r])^2,{r,0,(10^6)*Dcore/2}];

(* Cladding mode structure with matched boundary condition *)
BoundaryCondition3 = BesselJ[0,Kt3*(10^6)*Dcore/2]/
            BesselK[0,Gam3*(10^6)*Dcore/2];

Mode3Clad=Plot[(BoundaryCondition3)^2
         (BesselK[0,Gam3*r])^2,{r,(10^6)*Dcore/2,(10^6)*Dcore}];

(* Total pump mode picture *)

Show[Mode3Core,Mode3Clad,PlotRange->All]

(* Electric field equations for future use *)
ClearAll[CoreMode3,CoreMode3];
CoreMode3 = BesselJ[0,Kt3*r];
CladMode3 = (BoundaryCondition3)*BesselK[0,Gam3*r];

(*Constants in KMS*)
Plank = 6.6261 * 10^(-34);
SOL = 3 * 10^8;

(* Assume doping is uniform*)
NdDensity = 1.1*10^26;   (* m^-3, concentration of Yb in m^-3.*)
DopingRadius = Dcore/2;
CoreRadius = (Dcore/2)*10^6;

DopingEffectiveArea = Pi DopingRadius^2//N;

PumpArea = (2 Pi
    (NIntegrate[(10^-12)r*(CoreMode1)^2,{r,0,CoreRadius}]+
     NIntegrate[(10^-12)r*(CladMode1)^2,{r,CoreRadius,Infinity}]));

SeedArea = (2 Pi
    (NIntegrate[(10^-12)r*(CoreMode2)^2,{r,0,CoreRadius}]+
     NIntegrate[(10^-12)r*(CladMode2)^2,{r,CoreRadius,Infinity}]));

ASEArea = (2 Pi
    (NIntegrate[(10^-12)r*(CoreMode3)^2,{r,0,CoreRadius}]+
     NIntegrate[(10^-12)r*(CladMode3)^2,{r,CoreRadius,Infinity}]));

PumpEffectiveArea = (2 Pi
    (NIntegrate[(10^-12)r*(CoreMode1)^2,{r,0,CoreRadius}]));

SeedEffectiveArea = (2 Pi
    (NIntegrate[(10^-12)r*(CoreMode2)^2,{r,0,CoreRadius}]));

ASEEffectiveArea = (2 Pi
    (NIntegrate[(10^-12)r*(CoreMode3)^2,{r,0,CoreRadius}]));

PumpOverlap = (PumpEffectiveArea/PumpArea)

SeedOverlap = Abs[(SeedEffectiveArea/SeedArea)]

ASEOverlap = Abs[(ASEEffectiveArea/ASEArea)]

(*Effective Areas For Saturation Power Calculations*)
PumpEffectiveArea = ((2 Pi ((NIntegrate[(10^-12) r*(CoreMode1)^2, {r,0, CoreRadius}]) +
(NIntegrate[(10^-12) r*(CladMode1)^2, \{r, CoreRadius, 100 CoreRadius}])))^2)/(2 Pi (NIntegrate[(10^-
12) \r*(CoreMode1)^4, {r, 0, CoreRadius}]) + 2 Pi (NIntegrate[(10^-12) r*(CladMode1)^4, {r, CoreRadius,
100 CoreRadius}]))

SeedEffectiveArea = Abs[((2 Pi ((NIntegrate[(10^-12) r*(CoreMode2)^2, {r, 0,CoreRadius}]) +
(NIntegrate[(10^-12) r*(CladMode2)^2, {r,CoreRadius, 100 CoreRadius}])))^2)/(2 Pi (NIntegrate[(10^-12)
\r*(CoreMode2)^4, {r, 0, CoreRadius}]) + 2 Pi (NIntegrate[(10^-12) r*(CladMode2)^4, {r, CoreRadius,
100 CoreRadius}]))]

ASEEffectiveArea = Abs[((2 Pi ((NIntegrate[(10^-12) r*(CoreMode3)^2, {r, 0,CoreRadius}]) +
(NIntegrate[(10^-12) r*(CladMode3)^2, {r,CoreRadius, 100 CoreRadius}])))^2)/(2 Pi (NIntegrate[(10^-12)
\r*(CoreMode3)^4, {r, 0, CoreRadius}]) + 2 Pi (NIntegrate[(10^-12) r*(CladMode3)^4, {r, CoreRadius, 100
CoreRadius}]))]

(*Constant*)

FLifetime = 0.85 * 10^-3; (*Lifetime of fiber in use*)

(*P is for pump, S is for lasing signal. *)
PAbsCrsSec = 2.5 * 10^(-24); (* at 978nm *)
SAbsCrsSec =8.91 * 10^(-27);   (* *)
SEmCrsSec =3.10 * 10^(-25);
PEmCrsSec =   2.44 * 10^(-24);
AAbsCrsSec = 0 * 10^(-25); (*ASE can be ignored *)
AEmCrsSec = 0.1 * 10^(-25);   (* ASE can be ignored *)

(*Find the inversion threshold *)
ClearAll[PumpPin,Manji,Helicalization]

(* Attenuation constants in m^-1 *)
SAbsCoeff = (NdDensity)*(1)*(SAbsCrsSec)SeedOverlap
PAbsCoeff = (NdDensity)*(1)*(PAbsCrsSec)PumpOverlap
AAbsCoeff = (NdDensity)*(1)*(AAbsCrsSec)ASEOverlap

(*P denotes Pump and S denotes seed. *)
PSSatPhot = (SeedEffectiveArea)/((SeedOverlap)*
         (FLifetime)*((SAbsCrsSec)+(SEmCrsSec)))/10 ^16 ;

PPSatPhot = (PumpEffectiveArea)/((PumpOverlap)*
         (FLifetime)*((PAbsCrsSec)+(PEmCrsSec)))/10 ^16 ;

 ASatPhot = (ASEEffectiveArea)/((ASEOverlap)*
         (FLifetime)*((AAbsCrsSec)+(AEmCrsSec)))/10 ^16 ;

Delta = PSSatPhot/PPSatPhot;
GMAX = Exp[((PAbsCoeff/Delta)   -   SAbsCoeff)FiberLength];

(* These are saturation intensities in Watts *)
PSSatPow = 10 ^ 16 PSSatPhot Plank SOL/Lambda2;
PPSatPow = 10 ^ 16 PPSatPhot Plank SOL/Lambda1;
ASatPow = 10 ^ 16   ASatPhot Plank SOL/Lambda3;

(* Here we estimate the input powers
  for a forward pump direction (i.e. co-propagating beams) *)
ClearAll[A3,A1,A2,Fiberlength,SeedPinPhot,PumpPinPhot,ASEPinPhot];

(*Convert to photon flux for rate equations*)
SeedPinPhot[SeedPin_] := SeedPin Lambda2/(Plank SOL)/10 ^16 ;
ASEPinPhot[ASEPin_] := ASEPin Lambda3/(Plank SOL)/10^16;
(*PumpPinPhot[PumpPin_] := PumpPin Lambda1/(Plank SOL)/10^0;*)
PumpPinPhot= Eps1P PumpPin Lambda1/(Plank SOL)/10 ^16;   (* Pump Loss Built in here *)

(*Laser calculations*)
PLaser = (1 - R2) Eps2 PRout;

```
R1 = 0.00054;    (* FBG #1 reflectivity *)
R2 = 0.5068;    (* FBG #2 reflectivity *)
R = Sqrt[R1 R2];
 (* Background loss  *)
Eps2 =0.891; (*Loss at end 2*)

FiberLength =  0.75;    (* Length of Yb-doped fiber *)
Eps1 = 0.891;  (*Loss at end 1*)
Eps1P = Exp[0.0 * FiberLength]  (* Background Loss of Fiber *)

Eps = Eps1 Eps2;
Teff = (1 - Eps2^2  R2)+(1 - Eps1^2  R1)Eps2^2  R2  *(1/(Eps R))



LaserOutput = {};
PumpPower = {};
Do[

  PumpPin = i;


  LaserPhot = PROUT/.FindRoot[PSSatPhot  (SAbsCoeff FiberLength - Log[Eps R] + (Teff
PROUT)/PSSatPhot)  -  PumpPinPhot(1 - ((GMAX Eps R)^(-Delta)) Exp[PROUT  Teff((Delta/PSSatPhot) -
(1/PPSatPhot))])==0,{PROUT,1000}];

  PowerOut = 10^16  (Plank  SOL/Lambda2)*LaserPhot;
  AppendTo[PumpPower,i];
  AppendTo[LaserOutput,(1 - R2)Eps2  PowerOut],
  {i,0.00,0.200,0.001}];

aaaa = ListPlot[Transpose[{1000*PumpPower,1000*LaserOutput}],Joined->True,PlotStyle-
>{Black,Thickness[0.01]},BaseStyle->{FontColor->Black,FontWeight->"Bold",FontFamily-
>"Times",FontSize->14},Frame->True, FrameLabel->{"Pump Power (mW)", "Output Power (mW)"}]
```

(*Slope Efficiency Calculations*)
```
TheoreticalSlopeNoLoss =100 (Lambda1/Lambda2)  Eps2 (1 - R2) (1/Teff) (PSSatPhot/PSSatPhot)(1 -
(GMAX  Eps R)^(-Delta))
aa = Length[LaserOutput];
CalculatedSlope = 100(LaserOutput[[aa]]-LaserOutput[[aa-100]])/(PumpPower[[aa]]-PumpPower[[aa-
100]])
```